IEEE Access
Multidisciplinary | Rapid Review | Open Access Journal

Received 7 October 2024, accepted 30 October 2024, date of publication 5 November 2024, date of current version 15 November 2024.

Digital Object Identifier 10.1109/ACCESS.2024.3491759

RESEARCH ARTICLE

Active Disturbance Rejection and Voltage Stabilization Control Strategy for Energy Storage Converter in Microgrid Based on Observation State Correction

XUESONG ZHOU[1], YANAN JING[1], YOUJIE MA[1], XIN WANG[1], LONG TAO[1], AND HULONG WEN[2]

[1]Tianjin Key Laboratory of New Energy Power Conversion, Transmission, and Intelligent Control, Tianjin University of Technology, Tianjin 300384, China
[2]Tianjin Ruineng Electric Company Ltd., Tianjin 300385, China

Corresponding author: Youjie Ma (sjteam2022@163.com)

This work was supported by the Key Project of National Natural Science Foundation of China under Grant U23B20142.

ABSTRACT The output fluctuation of the high proportion of photovoltaic new energy requires introducing energy storage units for compensation and adjustment, but the voltage stability performance of energy storage port converters under complex working conditions is often not effectively guaranteed. Therefore, this paper proposes an active disturbance rejection voltage stabilization strategy considering observation state correction for energy storage port converters. By deriving the high-precision paradigm of observation deviation, the important structural factors of observation deviation in the system are pointed out, and the ignored high-order terms of deviation are compensated into the observer to achieve accurate and rapid convergence of tracking deviation. Furthermore, through the theoretical analysis of the strategy in four dimensions of stability performance, tracking performance, anti-disturbance performance, and robust performance, the reasons why the strategy can effectively improve the anti-disturbance and robustness of the converter are explained. Finally, the simulation and experimental results jointly demonstrate that the strategy performs better anti-disturbance and robust-ness performance than traditional active disturbance rejection control under various complex working conditions of microgrids, which is of great significance for improving the stability of microgrid operation.

INDEX TERMS Active disturbance rejection control, anti-disturbance performance, energy storage converter, microgrid, robust performance, status correction.

I. INTRODUCTION

The power system with ''a high proportion of new energy and a high proportion of power electronic equipment'' characteristics is an important tool to promote the green transformation of energy structure and a key carrier to achieve the dual carbon goals [1], [2]. As an important part of the new power system, the DC microgrid is of great significance in solving the energy consumption problem caused by the ''fragmented'' access to new energy such as photovoltaics. However, natural factors cause the output of new energy to have inherent characteristics of volatility, randomness, and indirectness [3], [4]. Large-scale introduction will bring new stability problems, such as frequent fluctuations in DC bus voltage and difficulty in maintaining source-load power balance. The hybrid energy storage (HES) system with battery (BAT) and supercapacitor (SC) as the core has the functions of peak shaving, providing excess power, and stabilizing DC bus voltage [5]. Therefore, the introduction of hybrid energy storage units becomes particularly important for the stable operation of microgrids with a high proportion of new energy. The stable operation of the power grid can be effectively achieved by efficiently controlling the power electronic devices as the hub of energy storage and bus energy

The associate editor coordinating the review of this manuscript and approving it for publication was Arturo Conde.

transmission [6], [7]. At present, various advanced control strategies have been introduced into hybrid energy storage interface bidirectional DC-DC converters (BDC) to better solve the more complex power quality problems, oscillation overshoot, and other operating stability problems brought by new energy.

The first is the classic proportional-integral (PI) control strategy, the core concept is ''using deviation to eliminate deviation''. Its simple operation principle brings good effect but stability problems caused by the contradiction between its own rapidity and overshoot can easily cause stability problems such as large fluctuation amplitude of system output [8]. Therefore, some studies have integrated fuzzy control into the PI strategy and designed fuzzy rules to improve the anti-disturbance performance of the converter, which has improved the DC bus voltage quality to a certain extent, but the ripple control effect is not significant [9]. The article [10] introduces a meta-heuristic algorithm based on the traditional PI control strategy for the buck converter, aiming to solve the problems of poor anti-disturbance performance and sensitivity to noise interference of the converter, but the introduction of the algorithm will inevitably bring more parameters that need to be adjusted. The second is the adaptive control strategy (AC), the core concept is to achieve stable control of the system by estimating and adjusting the system parameters. A study proposed a dual-mode digital controller with a Gaussian adaptive duty cycle switch for step-down DC-DC converters, which improved the dynamic performance of the converter [11]. Sun and his team integrated the adaptive strategy with droop control and improved the adaptive algorithm through the system output deviation, which improved the voltage regulation performance of the energy storage system to a certain extent, but the effect of suppressing disturbances with excessive fluctuations was limited [12]. The third is the active disturbance rejection control (ADRC) strategy, which relies on the internal extended state observer (ESO) to observe the state of the controlled object and the unknown disturbance signals of the system in real time. Therefore, it no longer relies on the establishment of an accurate mathematical model of the controlled object and has low model dependence. ADRC is divided into two types: nonlinear and linear. Nonlinear ADRC was proposed before linear control. It has strong robustness and high disturbance rejection. It has also been applied to various studies such as generators [13] and enhanced permanent magnet synchronous motors (PMSM) [14], [15]. However, due to the nonlinear and non-smooth feedback structure in ADRC [16], its theoretical analysis is difficult, and many control parameters need to be adjusted in the application. Therefore, the concept of linear ADRC was proposed, which greatly simplified the analysis and implementation of nonlinear ADRC. After that, many studies have made various improvements to the linear ADRC strategy, such as related studies have improved the second-order cascade structure of the active disturbance rejection control and the observer sequence correction fusion improvement, taking into account the bus voltage stability and rapid response, and can quickly smooth the bus voltage fluctuations [17], [18].

The presence of nonlinear elements and parasitic parameters in the BDC circuit makes its mathematical model nonlinear [19]. Linear ADRC (LADRC) stands out from other strategies due to its strong robustness and low dependence on the model, and is widely used in the control of energy storage converters [20]. The main components of the LADRC are LESO and linear state error feedback control law (LSEF). The core concept is to use linear ESO (LESO) to observe the total disturbance information in the system in real time before the output of the microgrid control system has a significant fluctuation, and use the LSEF module to dynamically compensate for it, thereby improving the system's anti-disturbance and rapidity [21]. Studies have shown that the mismatch between the controlled object model and the observer order will affect the tracking accuracy of the observer in TR-LADRC, generate tracking errors, and cause the system to produce non-ideal characteristics such as large output overshoot and time lag in some complex working conditions [22]. It will also introduce high-frequency noise, which will have an adverse effect on the output power quality and power safety [23]. Therefore, in conventional LADRC, there is a contradiction between improving the observer's estimation performance of the total disturbance by increasing the magnitude of the parameters and suppressing disturbances such as system noise. If the tracking accuracy of the observer can be improved by improving the TR-LADRC strategy and accurate tracking of system disturbances can be achieved, the observed total disturbance can be effectively suppressed through the linear state error feedback control rate.

To address this problem, the current improvement research in the field of active disturbance rejection control mainly includes two mainstream solutions: model information compensation with LADRC (MI-LADRC) and cascade compensation with LADRC (CA-LADRC). Representative studies of MI-LADRC ideas are as follows: Ma extracts model information and compensates it into the observer coefficient matrix to achieve a more accurate estimation of the total disturbance [24]. Article [25] constructs a dynamic function containing model information to reduce the total disturbance component, effectively reducing the observation burden of LESO and improving the system's resistance to disturbance. Article [26] describes the controlled system model as an n-order form and designs n active disturbance rejection controllers based on n-state feedback quantities, which improves the tracking performance. However, the increase in the number of controllers not only burdens the system operation, but also introduces additional disturbances. Representative studies of CA-LADRC ideas are as follows: some studies have introduced a front-stage observer to observe the total disturbance at the first level, and compensated it in the back-stage observer to form a cascade structure, and verified

that this strategy can improve the power quality of the system [27], [28]. Liu formed a compensation amount through a voltage and current double closed-loop and fed it back to the observer to compensate for the deviation, and verified that the disturbance estimation and suppression performance of this strategy were improved under various working conditions, and the system robustness performance was also greatly improved [29]. The paper [30] introduced a feedforward compensation link to the voltage loop of the photovoltaic storage system to compensate for the system output error, and designed an inertia weight fac-tor as an auxiliary parameter adjustment tool for self-disturbance rejection to adjust the parameters, and finally achieved an effective improvement in the system's anti-disturbance performance. In contrast, the second solution idea is obviously less restricted, the parameters are easy to configure, and the engineering applicability is stronger.

However, it should be pointed out that although the above two improvement ideas have improved the performance of LADRC to a certain extent, they are improvements to the external environment of LESO, and the performance is improved by reducing the observation burden. They do not analyze and improve the performance from the internal structure of LESO based on the observation deviation, which greatly limits the strategy's guarantee for the dynamic performance of the energy storage converter.

Given the above problems, this paper takes the BDC of the DC microgrid hybrid energy storage port as the controlled object, focuses on the core internal structure of the observer unit of the active disturbance rejection controller, and proposes an improved LADRC based on the observation state correction (SC-LADRC) to solve the complex problem that the output of the converter of the microgrid energy storage port is easily fluctuated due to disturbances. The main contributions of this improved active disturbance rejection control strategy are:

(1) By reconstructing the model structure of LESO, the control effect of the LADRC strategy is effectively improved. The SC-LADRC strategy proposed by this article solves the observation bias paradigm of TR-LADRC, retrieves the high-precision deviation component lost by the observer, and compensates it into LESO, achieving the correction of the observation volume and the tracking accuracy of the observer. The improvement shows significant advantages over TR-LADRC when observing multiple complex disturbance functions, which significantly improves the comprehensive performance of the LADRC strategy.

(2) The SC-LADRC strategy proposed in this paper is applied to the control of the energy storage interface converter, under the typical complex external working conditions of the system where the photovoltaic output power fluctuates greatly and the load-side power demand changes greatly, the stable control of the bus voltage and the balanced regulation of the system power are effectively achieved. Compared with the TR-LADRC strategy and the CA-LADRC strategy, the SC-LADRC strategy has a more significant voltage stabilization effect and a wider range of applications. It can better suppress the new stability problems brought about by the introduction of large-scale photovoltaic new energy, including the complex problems of frequent fluctuations in the DC bus voltage and the difficulty in maintaining the source-load power balance.

(3) Under the condition of internal parameter perturbation of the converter system, the SC-LADRC strategy still has stronger robustness performance than the TR-LADRC strategy and CA-LADRC strategy. By introducing two internal disturbance conditions, namely, irregular perturbation of the converter internal parameters and irregular change of the controller internal parameters, to the converter system under the improved control strategy, it is found through comparative analysis that the output signal of the energy storage converter under the control of the SC-LADRC strategy has smaller fluctuation and shorter fluctuation duration, and has stronger robustness.

Through the dual-dimensional verification of the SC-LADRC system in the time-frequency domain theoretical analysis and simulation experiments, the correctness and effectiveness of the SC-LADRC strategy proposed are demonstrated. In the DC microgrid operation scenarios with strong uncertainty, multiple complex interferences, and variable coupling, the SC-LADRC strategy is significantly better than the TR-LADRC strategy and CA-LADRC strategy and has relatively superior engineering application potential.

II. MICROGRID STRUCTURE AND ENERGY STORAGE CONVERTER MODELING

A. ENERGY TRANSFER PRINCIPLE IN MICROGRID

A DC microgrid is mainly composed of a renewable energy power generation unit, a hybrid energy storage unit, an energy transmission hub, a load unit, etc. It can be connected to an external large power grid or operate in an isolated grid [31]. Its typical structure is shown in Figure 1.

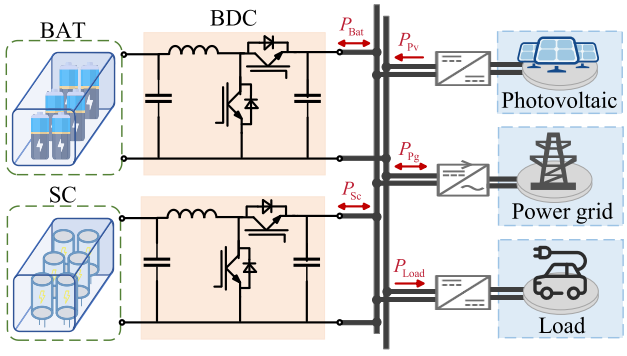

FIGURE 1. Typical structure of DC microgrid.

As shown in Fig. 1, the photovoltaic power generation unit provides energy for the DC bus for consumption on the load side; the hybrid energy storage unit composed of batteries and supercapacitors is connected to the DC bus through BDC to compensate for the fluctuation of photovoltaic output and

provide the energy required by the load when the photovoltaic production is insufficient. Therefore, the energy conservation principle of the DC microgrid can be described as:

$$\begin{cases} P_{\mathrm{HES}} = P_{\mathrm{Bat}} + P_{\mathrm{Sc}} \\ P_{\mathrm{HES}} + P_{Pv} = P_{\mathrm{Load}} + P_{\mathrm{Grid}} \end{cases} \tag{1}$$

where P_{HES} is the output power of the HES unit, which is com-posed of the output power of the battery group P_{Bat} and the output power of the super-capacitor group P_{Sc}; P_{Pv} is the output power of the photovoltaic unit; P_{Load} is the load power consumption; P_{Grid} represents the power of the large power grid. At the same time, $P_{\mathrm{HES}} > 0, P_{\mathrm{Bat}} > 0, P_{\mathrm{Sc}} > 0$ represent that the energy storage device is in a discharging state.

B. HES PORT BDC CIRCUIT MODELING

The BDC topology of the DC microgrid energy storage port is shown in Figure 2, where v_{h} is the terminal voltage of the hybrid energy storage device;i_{h} is the terminal current of the HES device; C_1 and C_2 are the HES side capacitor and the DC bus side capacitor respectively; v_{C1} and v_{C2} are the energy storage side and DC bus side capacitor voltages respectively; L is the filter inductor; i_{L} is the filter inductor current; Q_1 and Q_2 are switch tubes; D_1 and D_2 are reverse diodes; v_{d} is the DC bus side voltage; i_{d} is the DC bus side current.

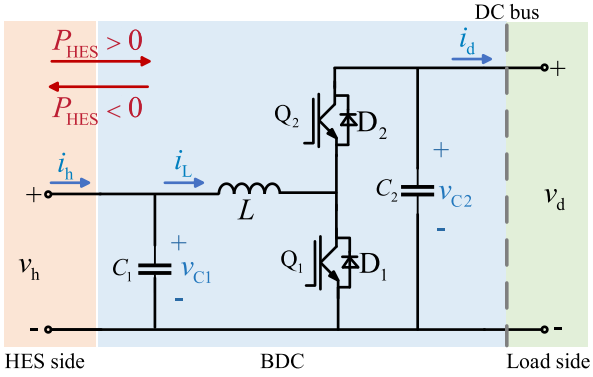

FIGURE 2. Energy storage port BDC circuit topology.

Based on the opening and closing of Q_1, Q_2, D_1, and D_2, the converter working modes are divided into two types: BUCK mode and BOOST mode. The duty cycles of the two modes are defined as d_1 and d_2 respectively, and the inductor current $i_{\mathrm{L}}(t)$, the capacitor terminal voltage $v_{\mathrm{C1}}(t)$ on the energy storage side, and the capacitor terminal voltage $v_{\mathrm{C2}}(t)$ on the DC bus side are selected as state variables. The mathematical models of the two modes are established based on the state space averaging method [32].

1) BUCK MODE

State 1: switch tube Q_2 is turned on, Q_1 is turned off, reverse diodes D_1 and D_2 are cut off. According to Kirchhoff's Current and Voltage Law (KCL) and Kirchhoff's Voltage Law (KVL), the mathematical model of state 1 in BUCK mode is established as follows:

$$\begin{cases} \dfrac{\mathrm{d}v_{\mathrm{C1}}(t)}{\mathrm{d}t} = \dfrac{1}{C_1} i_{\mathrm{L}}(t) - \dfrac{1}{R_{\mathrm{h}} C_1} v_{\mathrm{h}}(t) \\ \dfrac{\mathrm{d}v_{\mathrm{C2}}(t)}{\mathrm{d}t} = -\dfrac{1}{C_2} i_{\mathrm{L}}(t) + \dfrac{1}{R_{\mathrm{d}} C_2} v_{\mathrm{d}}(t) \\ \dfrac{\mathrm{d}i_{\mathrm{L}}(t)}{\mathrm{d}t} = \dfrac{1}{L}[v_{\mathrm{C2}}(t) - v_{\mathrm{C1}}(t)] \end{cases} \tag{2}$$

where: R_{h} and R_{d} are the equivalent internal resistance of the energy storage side and the bus side, respectively

State 2: Switch tubes Q_1 and Q_2 are turned off, reverse diodes D_1 are turned on, and D_2 is cut off. The mathematical model of state 2 in BUCK mode is established based on KCL and KVL as follows:

$$\begin{cases} \dfrac{\mathrm{d}v_{\mathrm{C1}}(t)}{\mathrm{d}t} = \dfrac{1}{C_1} i_{\mathrm{L}}(t) - \dfrac{1}{R_{\mathrm{h}} C_1} v_{\mathrm{h}}(t) \\ \dfrac{\mathrm{d}v_{\mathrm{C2}}(t)}{\mathrm{d}t} = \dfrac{1}{R_{\mathrm{d}} C_2} v_{\mathrm{d}}(t) \\ \dfrac{\mathrm{d}i_{\mathrm{L}}(t)}{\mathrm{d}t} = -\dfrac{1}{L} v_{\mathrm{C1}}(t) \end{cases} \tag{3}$$

The state space average mathematical model of the two states is established by combining equations (2) and (3):

$$\begin{bmatrix} \dot{v}_{\mathrm{C1}} \\ \dot{v}_{\mathrm{C2}} \\ \dot{i}_{\mathrm{L}} \end{bmatrix} = \begin{bmatrix} 0 & 0 & \dfrac{1}{C_1} \\ 0 & 0 & -\dfrac{d_1}{C_2} \\ -\dfrac{1}{L} & \dfrac{d_1}{L} & 0 \end{bmatrix} \begin{bmatrix} v_1 \\ v_2 \\ i_{\mathrm{L}} \end{bmatrix} + \begin{bmatrix} 0 & -\dfrac{1}{R_{\mathrm{h}} C_1} \\ \dfrac{1}{R_{\mathrm{d}} C_2} & 0 \\ 0 & 0 \end{bmatrix} \begin{bmatrix} v_{\mathrm{d}} \\ v_{\mathrm{h}} \end{bmatrix} \tag{4}$$

By using the small signal modeling method, the transfer function of the interface converter on the HES side of the DC microgrid in BUCK mode can be obtained as follows:

$$\begin{cases} G_{\mathrm{id1}}(s) = \dfrac{i_{\mathrm{L}}(s)}{d_1(s)} = \dfrac{v_{\mathrm{d}}(C_1 R_{\mathrm{h}} s + 1)}{L C_1 R_{\mathrm{h}} s^2 + L s + R_{\mathrm{h}}} \\ G_{\mathrm{vd1}}(s) = \dfrac{v_{\mathrm{h}}(s)}{d_1(s)} = \dfrac{v_{\mathrm{d}} R_{\mathrm{h}}}{L C_1 R_{\mathrm{h}} s^2 + L s + R_{\mathrm{h}}} \end{cases} \tag{5}$$

2) BOOST MODE

State 1: switch tube Q_1 is turned on, Q_2 is turned off, and reverse diodes D_1 and D_2 are cut off. The mathematical model of state 1 is established based on KCL and KVL as follows:

$$\begin{cases} \dfrac{\mathrm{d}v_{\mathrm{C1}}(t)}{\mathrm{d}t} = -\dfrac{1}{C_1} i_{\mathrm{L}}(t) - \dfrac{1}{C_1 R_{\mathrm{h}}} v_{\mathrm{h}}(t) \\ \dfrac{\mathrm{d}v_{\mathrm{C2}}(t)}{\mathrm{d}t} = -\dfrac{1}{C_2 R_{\mathrm{d}}} v_{\mathrm{d}}(t) \\ \dfrac{\mathrm{d}i_{\mathrm{L}}(t)}{\mathrm{d}t} = \dfrac{1}{L} v_{\mathrm{C1}}(t) \end{cases} \tag{6}$$

State 2: Switch tubes Q_1 and Q_2 are turned off, reverse diodes D_2 are turned on, and D_1 is turned off. The

mathematical model of state 2 is established as follows:

$$\begin{cases} \dfrac{\mathrm{d}v_{C1}(t)}{\mathrm{d}t} = -\dfrac{1}{C_1} i_L(t) \\ \dfrac{\mathrm{d}v_{C2}(t)}{\mathrm{d}t} = \dfrac{1}{C_2} i_L(t) - \dfrac{1}{C_2 R_d} v_d(t) \\ \dfrac{\mathrm{d}i_L(t)}{\mathrm{d}t} = \dfrac{1}{L} v_{C1}(t) - \dfrac{1}{L} v_{C2}(t) \end{cases} \tag{7}$$

The state space average mathematical model of the two states in BOOST mode is established by combining equations (6) and (7):

$$\begin{bmatrix} \dot{v}_{C1} \\ \dot{v}_{C2} \\ \dot{i}_L \end{bmatrix} = \begin{bmatrix} 0 & 0 & -\dfrac{1}{C_1} \\ 0 & 0 & \dfrac{1-d_2}{C_2} \\ \dfrac{1}{L} & -\dfrac{1-d_2}{L} & 0 \end{bmatrix} \begin{bmatrix} v_{C1} \\ v_{C2} \\ i_L \end{bmatrix} + \begin{bmatrix} 0 & -\dfrac{1}{R_h C_1} \\ -\dfrac{1}{R_d C_2} & 0 \\ 0 & 0 \end{bmatrix} \begin{bmatrix} v_d \\ v_h \end{bmatrix} \tag{8}$$

The state space averaging method and small signal modeling method are also used to model the DC microgrid energy storage side interface converter in BOOST mode.

$$\begin{cases} G_{id2}(s) = \dfrac{i_L(s)}{d_2(s)} = \dfrac{v_d(C_2 R_d s + 1) + (1-d_2) R_d I_L}{L C_2 R_d s^2 + L s + R_d (1-d_2)^2} \\ G_{vd2}(s) = \dfrac{v_d(s)}{d_2(s)} = \dfrac{v_d R_d (1-d_2) - L I_L R_d s}{L C_2 R_d s^2 + L s + R_d (1-d_2)^2} \end{cases} \tag{9}$$

where I_L is the DC value of the inductor current at the steady-state operating point of the system generated during the small signal modeling process.

III. DESIGN AND ANALYSIS OF SC-LADRC STRATEGY

A. ANALYSIS OF PROBLEMS WITH TR-LADRC STRATEGIES

A high-order system with perturbations can be described as follows:

$$y^{(n)}(t) = q[y(t), y^{(1)}(t), y^{(2)}(t), \cdots, y^{(n-1)}(t), \omega(t)] + bu(t) \tag{10}$$

where: $y(t)$ is the system output; $q(\cdot)$ is the coupling relationship between the state variables in the system; $\omega(t)$ is the external disturbance to the system; b is the controller gain (cannot be accurately obtained), $b = v_d \cdot (LC_1)^{-1}$ is in BUCK step-down mode, $b = v_d \cdot (LC_2)^{-1}$ is in BOOST step-up mode; $u(t)$ is the control quantity output by the LSEF module, which is applied to the controlled energy storage converter.

In the traditional second-order LADRC control, the controlled object is equivalent to a double-integral series form. At the same time, since the system parameter b cannot be accurately estimated, the parameter b_0 is introduced to represent the part of b that is accurately estimated. The uncontrollable part of the system is defined as the total disturbance $f(t)$, which is the sum of the external disturbance and the internal uncertainty component of the system:

$$\begin{aligned} f(t) = q[y(t), y'(t), y''(t), y^{(3)}(t) \cdots, y^{(n-1)}(t), \omega(t)] \\ + (b - b_0)u(t) - y^{(n)}(t) + y''(t) \end{aligned} \tag{11}$$

It is usually assumed that f is differentiable [33], and η is defined to represent the first derivative of f. The combined equations (10) and (11) simplify the high-order system to:

$$y''(t) = f(t) + b_0 u(t) \tag{12}$$

where: $y''(t)$ is the second derivative of the system output quantity $y(t)$. In the traditional second-order ADRC, state variables $x_1(t)$ and $x_2(t)$ are selected to describe the system output $y(t)$ and its first-order derivative $y'(t)$ respectively, and the expanded state variable $x_3(t)$ is selected to describe the total disturbance $f(t)$. Based on the selection of the above state variables, equation (12) is re-expressed in state space form:

$$\dot{x} = \mathbf{A}x + \mathbf{B}u + \mathbf{E}\eta \tag{13}$$

The matrices have the following meanings:

$$x = \begin{bmatrix} x_1 \\ x_2 \\ x_3 \end{bmatrix}, \mathbf{A} = \begin{bmatrix} 0 & 1 & 0 \\ 0 & 0 & 1 \\ 0 & 0 & 0 \end{bmatrix}, \mathbf{B} = \begin{bmatrix} 0 \\ b_0 \\ 0 \end{bmatrix}, \mathbf{E} = \begin{bmatrix} 0 \\ 0 \\ 1 \end{bmatrix}$$

According to the controlled object (13), the corresponding traditional third-order LESO is established:

$$\dot{\hat{x}}_T = \mathbf{A}\hat{x}_T + \mathbf{B}u + \mathbf{L}(y - \hat{x}_{T1}) \tag{14}$$

In equation 14, the matrices have the following meanings:

$$\hat{x}_T = \begin{bmatrix} \hat{x}_{T1} \\ \hat{x}_{T2} \\ \hat{x}_{T3} \end{bmatrix} \mathbf{L} = \begin{bmatrix} \beta_{T1} \\ \beta_{T2} \\ \beta_{T3} \end{bmatrix}$$

Among them, $\hat{x}_T$ represents the observation value of LESO on the BDC circuit, $\mathbf{L}$ represents the observer gain coefficient, and LESO can track the state variables of the BDC circuit by selecting appropriate gain values, that is: $\hat{x}_{T1} \to y$, $\hat{x}_{T2} \to \dot{y}$, $\hat{x}_{T3} \to f$.

Combining equations (13) and (14), the observation deviation of the traditional LESO on the controlled object can be calculated:

$$\begin{cases} \dot{e}_1 = e_2 - \beta_{T1} e_1 \\ \dot{e}_2 = e_3 - \beta_{T2} e_1 \\ \dot{e}_3 = -\eta - \beta_{T3} e_1 \end{cases} \tag{15}$$

where $e_{Ti} = \hat{x}_{Ti} - x_i (i = 1, 2, 3)$ represents the observation error of the observer on the state variable. Assuming that f is bounded under normal circumstances, and $|\eta(t)| \le \eta_0$, η_0 are positive constants [34], the system tends to be stable over time and satisfies: $\dot{e}_{Ti} = 0$. The three gain coefficients of the traditional LESO are configured as: $\beta_{T1} = 3\omega_o$, $\beta_{T2} = 3\omega_o^2$, $\beta_{T3} = \omega_o^3$, where ω_o is the bandwidth gain of the extended

state observer. Substituting it into equation (15), the observer observation deviation can be recalculated as:

$$\begin{cases} |e_1| \le \eta_0/\omega_o^3 \\ |e_2| \le 3\eta_0/\omega_o^2 \\ |e_3| \le 3\eta_0/\omega_o \end{cases} \tag{16}$$

As can be seen from equation (16), the estimation of the total disturbance by the traditional LESO still has a non-negligible error, and it is necessary to design a compensation link to correct it as much as possible. The most important thing about the observer is to make e_{T1}, which is directly related to the system output, approach zero quickly to achieve accurate output of the system. However, the control of $\hat{x}_{T1}, \hat{x}_{T2}, \hat{x}_{T3}$ by LESO is synchronous. According to equation (14), when e_{T1} approaches zero after control, it becomes difficult for $\hat{x}_{T3}$, which is also based on the e_{T1} structure, to converge. In this case, the traditional LESO can only achieve accurate observation of the state by increasing the order of magnitude of the observer gain matrix $\mathbf{L}$. However, if the observer parameters are too large, high-frequency noise interference will be introduced, which greatly reduces the system performance [35]. Therefore, it is obviously unreasonable to construct the total disturbance observation $\hat{x}_{T3}$, which is of great significance to the system control performance, through the e_{T1} structure that converges first. It is necessary to find a suitable convergence speed adjustment basis to reconstruct LESO, compensate for observation errors, and achieve rapid convergence of the observer to the system error observation term $\hat{x}_{T3}$.

B. SC-LADRC STRATEGY DESIGN

Based on the analysis of the important influencing factors of LESO observation deviation in TR-LADRC, the high-precision paradigm of observation deviation is further deduced from equations (14) and (15):

$$\begin{cases} \hat{x}_{T1} - x_1 = e_{T1} \\ \hat{x}_{T2} - x_2 = \dot{e}_{T1} + \beta_{T1} e_{T1} \\ \hat{x}_{T3} - x_3 = \ddot{e}_{T1} + \beta_{T1}\dot{e}_{T1} + \beta_{T2} e_{T1} \end{cases} \tag{17}$$

where e_{T1} represents the tracking error of the observer for the converter output voltage. It can be seen from equation (17) that the disturbance observation deviation contains the high-order component of e_{T1}, which is completely ignored in the construction of traditional LESO. The core of LADRC is to quickly and accurately estimate the total disturbance [36]. In order to improve the LESO observation accuracy and improve the overall performance of the LADRC system, the high-order component $\Delta\dot{\hat{x}}_{R3}$ that is ignored when the traditional LESO observes the total disturbance is compensated into $\dot{\hat{x}}_{T3}$. The compensated disturbance observation $\hat{x}_{R3}$ is as follows:

$$\begin{cases} \Delta\dot{\hat{x}}_{R3} = -\beta_{R3}[\ddot{e}_1 + \beta_{R1}\dot{e}_1 + (\beta_{R2} - 1)e_1] \\ \dot{\hat{x}}_{R3} = \dot{\hat{x}}_{T3} + \Delta\dot{\hat{x}}_{R3} = -\beta_{R3}(\ddot{e}_1 + \beta_{R1}\dot{e}_1 + \beta_{R2} e_1) \end{cases} \tag{18}$$

In equation (18), e_1 represents the tracking error of the observer for y, and β_{R1}, β_{R2}, and β_{R3} are the parameters that the observer needs to configure. The observation state compensation unit (OSCU) of LESO is constructed according to formula (18), and its specific structural framework is shown in Figure 3. Fig. 3 also illustrates the compensation principle of OSCU for traditional LESO. Drawing OSCU and its compensation principle together in Figure 3 can more clearly demonstrate the initial structure of SC-LADRC.

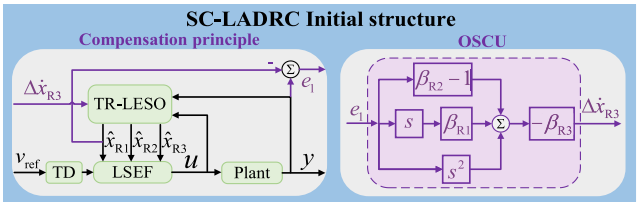

FIGURE 3. Observation state compensation unit.

Based on this, design an improved LESO structure based on disturbance observation state correction:

$$\begin{cases} \dot{\hat{x}}_R = \mathbf{A_R}\hat{x}_R + \mathbf{B_R}\mathbf{U} + \mathbf{L_R}(y - \hat{x}_{R1}) \\ \hat{y} = \mathbf{C_R}\hat{x}_R \end{cases} \tag{19}$$

where $\hat{y}$ represents the observation value of y, and the matrices have the following meanings:

$$\mathbf{A_R} = \begin{bmatrix} 0 & 1 & 0 \\ 0 & 0 & 1 \\ \beta_{R3} & 0 & -\beta_{R3} \end{bmatrix},$$

$$\mathbf{B_R} = \begin{bmatrix} 0 & 0 & 0 \\ b_0 & 0 & 0 \\ -b_0\beta_{R3} & -\beta_{R3} & \beta_{R3} \end{bmatrix},$$

$$\hat{x}_R = \begin{bmatrix} \hat{x}_{R1} & \hat{x}_{R2} & \hat{x}_{R3} \end{bmatrix}^T, \mathbf{L_R} = \begin{bmatrix} \beta_{R1} & \beta_{R2} & \beta_{R3} \end{bmatrix}^T,$$

$$\mathbf{U} = \begin{bmatrix} u & y & \ddot{y} \end{bmatrix}^T \mathbf{C_R} = \begin{bmatrix} 1 & 0 & 0 \end{bmatrix}$$

By comparing the improved LESO shown in Equation 19 with the traditional LESO shown in Equation 14, it can be seen that although their structures are similar, the fundamental coefficient matrices that determine the system structure and performance are completely different. That is, $\mathbf{A_R}$, $\mathbf{B_R}$, and $\mathbf{L_R}$ in Equation 19 are completely different from $\mathbf{A}$, $\mathbf{B}$,and $\mathbf{L}$ in Equation 14. Therefore, the improved LESO adds a high-precision disturbance compensation term $\Delta\dot{\hat{x}}_{R3}$ on the basis of $\dot{\hat{x}}_{T3}$, making the final disturbance observation term $\dot{\hat{x}}_{R3}$ completely different from $\dot{\hat{x}}_{T3}$ in the traditional LESO. This is the most essential difference between Equations 19 and 14, and also the core innovation point.

Furthermore, LSEF units effectively suppress the disturbance observed by LESO. Its specific structure is as follows:

$$\begin{cases} u(t) = \dfrac{u_0(t) - \hat{x}_{R3}(t)}{b_0} \\ u_0(t) = k_p[v_{ref}(t) - \hat{x}_{R1}(t)] + k_d[\dot{v}_{ref}(t) - \hat{x}_{R2}(t)] \end{cases} \tag{20}$$

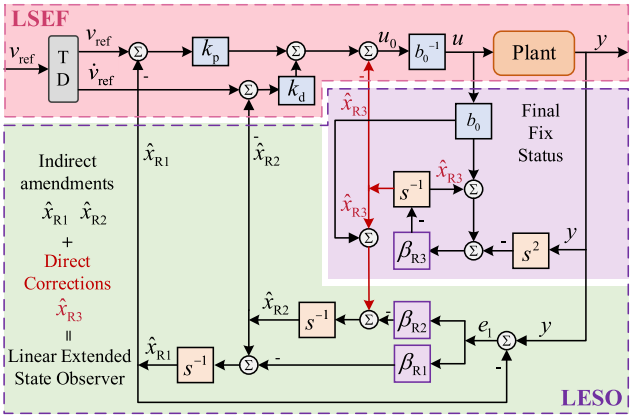

FIGURE 4. SC-LADRC overall structure diagram.

In equation (20), $u_0(t)$ denotes the primary quantity of $u(t)$, specifically, the primary control quantity output by the LSEF unit and applied to the BDC circuit. The final control quantity $u(t)$ is obtained by multiplying $u_0(t)$ with a coefficient b_0^{-1}. According to equations (19) and (20), the final structure of the SC-LADRC system is shown in Figure 4.

In Fig. 4, the OSCU has been fully compensated into LESO, and the final mode of LESO correction is obtained. Among them, since the compensation unit is a direct correction of $\hat{x}_{T3}$ in the TR-LADRC, $\hat{x}_{R3}$ in SC-LADRC is called a direct correction term; and $\hat{x}_{R1}$, $\hat{x}_{R2}$ are structurally improved with the help of the corrected $\hat{x}_{R3}$, so they are called indirect correction terms. The combination of the two constitutes the corrected improved LESO.

C. DESIGN OF PARAMETER SETTING RULES FOR SC-LADRC STRATEGY

Ignoring the observation deviation of LESO to the total disturbance, the controlled object (13) can be simplified to a series integral form, that is: $\ddot{y} = u_0$. Then the control rate can be simplified on this basis as:

$$\begin{cases} \dot{x}_u = \mathbf{A_{R1}} x_u + \mathbf{B_{R1}} u_0 \\ u_0 = k_p v_{ref} + k_d \dot{v}_{ref} + \mathbf{k_{R1}} \hat{x}_u \end{cases} \tag{21}$$

Among them, each matrix is specifically:

$$\mathbf{k_{R1}} = \begin{bmatrix} -k_p \\ -k_d \end{bmatrix}^T, \mathbf{A_{R1}} = \begin{bmatrix} 0 & 1 \\ 0 & 0 \end{bmatrix}, \mathbf{B_{R1}} = \begin{bmatrix} 0 \\ 1 \end{bmatrix},$$
$$x_u = \begin{bmatrix} x_1 \\ x_2 \end{bmatrix}, \hat{x}_u = \begin{bmatrix} \hat{x}_1 \\ \hat{x}_2 \end{bmatrix}$$

Furthermore, the LESO and LSEF parameters in SC-LADRC are configured according to the bandwidth parameterization method [37]. The core of the bandwidth parameterization method can be summarized as follows:

$$\begin{cases} \lambda_c(s) = \mathrm{eig}(\mathbf{A_{R1}} + \mathbf{B_{R1}} \mathbf{k_{R1}}) = (s + \omega_c)^n \\ \lambda_o(s) = \mathrm{eig}(\mathbf{A_R} - \mathbf{L_R} \mathbf{C_R}) = (s + \omega_o)^n \end{cases} \tag{22}$$

where $\lambda(s)$ represents the characteristic polynomial of the observer and control rate module; n is the system order under the specific description of the two units; $\mathbf{A_{R1}}, \mathbf{B_{R1}}, \mathbf{A_R}, \mathbf{C_R}$ are the system parameter matrices, $\mathbf{k_{R1}}, \mathbf{L_R}$ are the gain coefficient matrices that need to be adjusted; eig(·) represents the characteristic polynomial of the matrix; ω_c is the LSEF controller gain. The simultaneous equations (19), (21), and (22) can be used to obtain the parameter configuration adjustment rules for LESO and LSEF in SC-LADRC:

$$\begin{cases} k_p = \omega_c^2, k_d = 2\omega_c \\ \beta_{R1} = 2\omega_o, \beta_{R2} = \omega_o^2, \beta_{R3} = \omega_o \end{cases} \tag{23}$$

IV. SC-LADRC STRATEGY PERFORMANCE ANALYSIS

A. STABILITY ANALYSIS

The observation deviation of the LESO is defined as $\tilde{x}_i = x_i - \hat{x}_i$, and the gain coefficients in Eq. (23) are expressed as $\beta_{R1} = l_1\omega_o$, $\beta_{R2} = l_2\omega_o^2$, $\beta_{R3} = l_3\omega_o$, thus obtaining:

$$\begin{cases} \dot{\tilde{x}}_1 = \tilde{x}_2 - l_1\omega_o\tilde{x}_1 \\ \dot{\tilde{x}}_2 = \tilde{x}_3 - l_2\omega_o^2\tilde{x}_1 \\ \dot{\tilde{x}}_3 = -l_3\omega_o\ddot{\tilde{x}}_1 - l_1l_3\omega_o^2\dot{\tilde{x}}_1 - l_2l_3\omega_o^3\tilde{x}_1 + (\eta - \hat{\eta}) \end{cases} \tag{24}$$

Let $\varepsilon_i = \tilde{x}_i/\omega_o^{(i-1)}$, the estimation error of the improved LESO can be further described as:

$$\dot{\varepsilon} = \omega_o \mathbf{E_{R1}} \varepsilon + \mathbf{E_{R2}} \omega_o^{-2} [\dot{\eta}(x_i(t), f(t)) - \dot{\eta}(\hat{x}_i(t), f(t))] \tag{25}$$

Among them, each matrix is specifically:

$$\mathbf{E_{R1}} = \begin{bmatrix} -l_1\omega_o & \omega_o & 0 \\ -l_2\omega_o & 0 & \omega_o \\ 0 & 0 & -l_3\omega_o \end{bmatrix}, \varepsilon = \begin{bmatrix} \varepsilon_1 \\ \varepsilon_2 \\ \varepsilon_3 \end{bmatrix},$$
$$\mathbf{E_{R2}} = \begin{bmatrix} 0 \\ 0 \\ 1 \end{bmatrix}$$

Since $\eta(\hat{x}_i(t), f(t))$ is globally Lipschitz, there exists a constant $\omega_o > 0$ such that:

$$\lim_{t \to \infty} \tilde{x}_i(t) = 0 \tag{26}$$

From equation (26), we can see that Lyapunov's asymptotic stability theorem holds. When time tends to infinity, the observation deviation of the improved LESO is 0, so the improved LESO is convergent.

Assume that the goal of the controller is to make the output of the second-order controlled object (13) follow a given bounded reference signal $v_{ref}(t)$, and its differential signals $\dot{v}_{ref}(t)$ and $\ddot{v}_{ref}(t)$ are also bounded. Define $e_j = v_{refj} - x_j$(j = 1, 2), and equation (20) can be further expressed as:

$$u = b_0^{-1}[k_p(e_1 + \tilde{x}_1) - k_d(e_2 + \tilde{x}_2) + \tilde{x}_3 - x_3] \tag{27}$$

Assuming $e = \begin{bmatrix} e_1 & e_2 \end{bmatrix}^T \in R^n, \tilde{x} = \begin{bmatrix} \tilde{x}_1 & \tilde{x}_2 & \tilde{x}_3 \end{bmatrix}^T \in R^{n+1}$, we can get:

$$\dot{e}(t) = \mathbf{A_e} e(t) + \mathbf{A_{\tilde{x}}} \tilde{x}(t) \tag{28}$$

Among them, each matrix is specifically:

$$\mathbf{A_e} = \begin{bmatrix} 0 & 1 \\ -k_p & k_d \end{bmatrix}, \quad \mathbf{A_{\tilde{x}}} = \begin{bmatrix} 0 & 0 & 0 \\ -k_p & k_d & -1 \end{bmatrix}$$

Since k_p and k_d are chosen so that the characteristic polynomial $s^2 + (-k_p)s + k_d$ is Hurwitz, $\mathbf{A_e}$ is Hurwitz [38]. At the same time, it can be obtained from equation (26) that $\eta(\hat{x}_i(t), f(t))$ is globally Hurwitz with respect to $\hat{x}_i(t)$, so there exist constants $\omega_o > 0$ and $\omega_c > 0$ such that:

$$\lim_{t\to\infty} e_j(t) = 0 \tag{29}$$

According to Lyapunov theory, SC-LADRC is asymptotically stable, that is, stable in the engineering sense.

B. DISTURBANCE OBSERVATION PERFORMANCE ANALYSIS

The frequency domain functional relationship between the disturbance observation deviation and the disturbance of SC-LADRC can be obtained by combining equations (13), (19) and (20):

$$E_{SC}(s) = \hat{x}_{R3}(s) - F(s) = -\frac{s}{(s+\omega_o)} \cdot F(s) \tag{30}$$

Similarly, the frequency domain function relationship between the disturbance observation deviation and the disturbance under TR-LADRC can be calculated, as shown in the following equation:

$$E_{TR}(s) = \hat{x}_{T3}(s) - F(s) = -\frac{s^3 + 3\omega_o s^2 + 3\omega_o^2 s}{(s+\omega_o)^3} \cdot F(s) \tag{31}$$

Different types of disturbance functions are introduced for the two control systems, and the disturbance estimation performance is compared based on the observation error of the disturbance. The four different disturbance functions are: step function $f_1(t) = M$, ramp function $f_2(t) = Mt$, acceleration function $f_3(t) = Mt^2$, and periodic function $f_4(t) = M \sin \omega_1 t$, where M represents the function amplitude. The tracking error curves of the two control systems under the four disturbances are plotted as shown in Figure 5, and the specific values of the calculated errors are shown in Table 1. When the observer's error curve finally converges to the zero plane, it means that the observer has achieved accurate tracking of the system state variables; if the error curve cannot finally converge to the zero plane, the closer the curve is to the zero plane, the stronger the tracking performance. It can be seen from this that by comparing the three-dimensional response plane of disturbance between TR-LADRC strategy and SC-LADRC strategy, it is very intuitive to see the improvement of system performance by the improved strategy.

In Table 1, $M_1 = -MH_{e1}/2, H_i = (\omega_o t)^i, H_{e1} = e^{-\omega_o t}, H_{e2} = e^{\omega_o t}, g(\cdot), m(\cdot), n(\cdot)$ represent different functional relationships. It can be seen from Fig. 5 and Table 1 that under step disturbance, although both control systems can achieve zero-difference observation, the observation speed of the SC-LADRC system is significantly faster than that of the traditional control. This is because the improved strategy compensates for the anti-convergence factor $2H_1 + H_2$ in the traditional control. Under ramp disturbance, the traditional observer cannot achieve zero-difference observation, but the improved strategy can achieve fast zero-difference tracking because it does not have the high-order anti-convergence

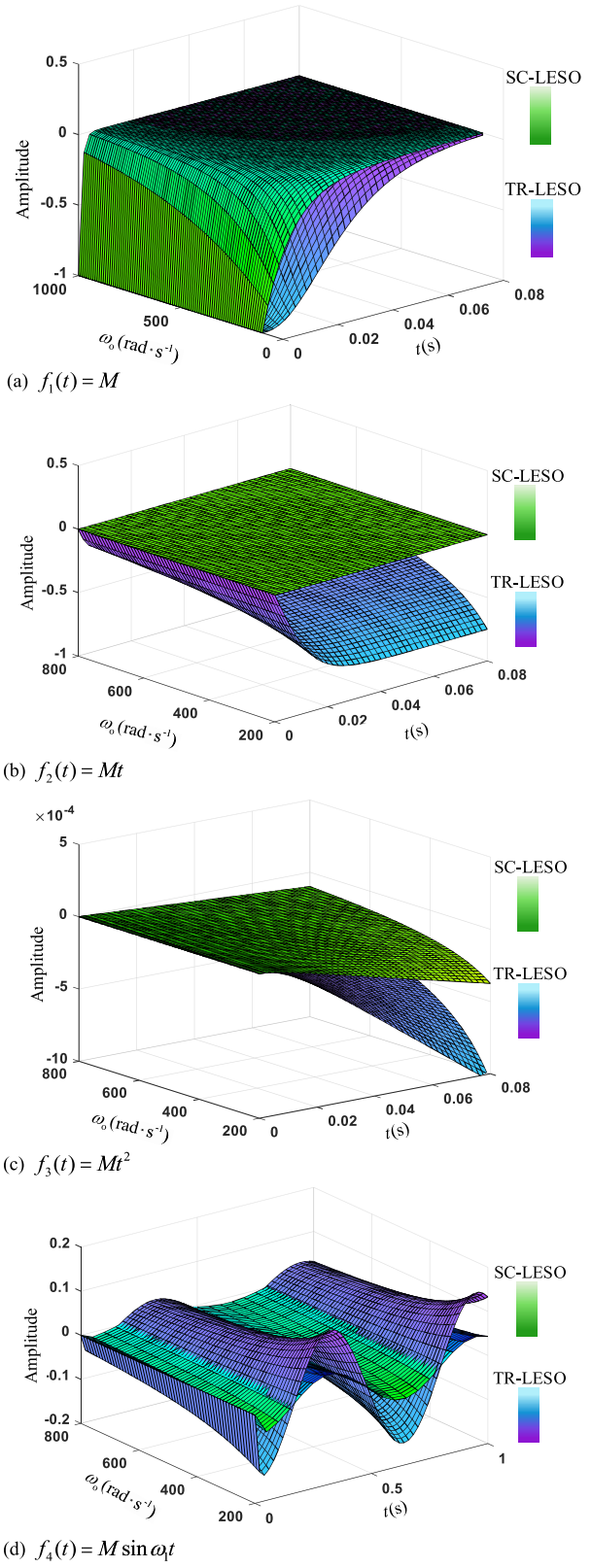

FIGURE 5. Comparison of observation performance for different disturbances.

TABLE 1. Numerical comparison of disturbance observation performance.

$f(t)$	TR-LADRC	SC-LADRC
M	$M_1(2+2H_1+H_2)$	$2M_1$
$M\cdot t$	$\frac{M_1(-6+6H_{e2}-4H_1-H_2)}{\omega_o}$	$\frac{2M_1(H_{e2}-1)}{\omega_o}$
$M\cdot t^2$	$\frac{M_1(12-12H_{e2}+6H_1+6H_2H_{e2}-H_3)}{\omega_o^2}$	$\frac{2M_1(1-H_{E2}+H_1H_{e2})}{\omega_o^2}$
$M\sin\omega_1 t$	$H_{e1}\cdot g_1(\omega_o)+m_1(\omega_o)\cdot n_1(\omega_1,t)$	$H_{e1}\cdot g_2(\omega_o)+m_2(\omega_o)\cdot n_2(\omega_1,t)$

factor $4H_1+H_2$ in the TR-LADRC. Under acceleration disturbance, the high change rate of the disturbance signal makes both of them diverge to a certain extent, but the divergence speed and degree of the improved strategy are much smaller than those of the traditional control. This is because the maximum anti-convergence high-order term $6H_2H_{e2}$ under the traditional strategy has been compensated by the improved strategy to a low-order form H_1H_{e2}. Under periodic disturbances, the periodic changes in the function result in periodic responses for both systems, but SC-LADRC has a smaller observation error amplitude for disturbances. From the numerical comparison, although the deviation forms of the two are consistent, function $m_2(\cdot)$ is 2-3 orders of magnitude smaller than $m_1(\cdot)$. Therefore, the error fluctuation amplitude of SC-LADRC to the disturbance observation is smaller. In summary, compared with the TR-LADRC strategy, the SC-LADRC strategy has higher observation accuracy for different forms of disturbance signals, and can achieve convergence of observation errors or significantly reduce the amplitude of observation errors in faster time and smaller deviations.

C. ANTIDISTURBANCE PERFORMANCE ANALYSIS

According to equations (19) and (20), the transfer function of the control variable with respect to the set value and the output signal can be obtained:

$$U(s)=b_0^{-1}G_{\text{ref}}(s)[k_{\text{p}}\cdot V_{\text{ref}}(s)-H_{\text{fb}}(s)\cdot Y(s)] \tag{32}$$

The internal transfer function is specifically expressed as:

$$\begin{aligned}G_{\text{ref}}(s)&=(s+\omega_{\text{o}})^3[s^3+(2\omega_{\text{o}}+k_{\text{d}})s^2+(\omega_{\text{o}}^2+2\omega_{\text{o}}k_{\text{d}}+k_{\text{p}})s]^{-1}\\ H_{\text{fb}}(s)&=[s^4+(k_{\text{d}}+2\omega_{\text{o}})s^3+(3k_{\text{p}}+3k_{\text{d}}\omega_{\text{o}}+\omega_{\text{o}}^2)s^2\\&\quad+(3k_{\text{p}}\omega_{\text{o}}+k_{\text{d}}\omega_{\text{o}}^2)s+k_{\text{p}}\omega_{\text{o}}^2]\omega_{\text{o}}(s+\omega_{\text{o}})^{-3}\end{aligned}$$

According to formula (32), the simplified equivalent model of SC-LADRC under disturbance state can be drawn as shown in Figure 6.

According to Fig. 6, the relationship between the system output signal y and the set value v_{ref} and the system total

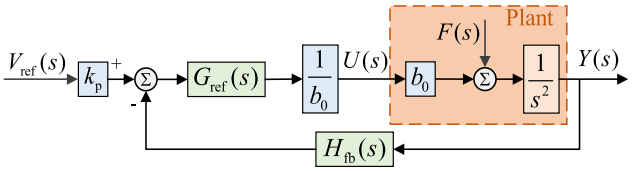

FIGURE 6. Disturbance-containing equivalent model of SC-LADRC.

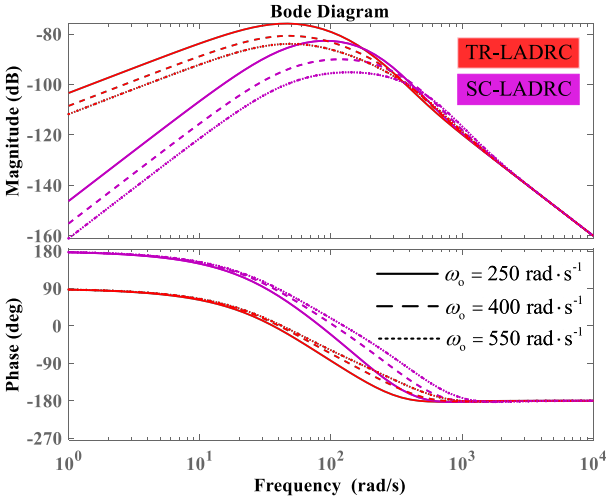

FIGURE 7. Disturbance suppression frequency domain characteristic comparison curve.

disturbance f can be obtained:

$$Y(s)=\frac{k_{\text{p}}G_{\text{ref}}(s)}{G_{\text{ref}}(s)H_{\text{fb}}(s)+s^2}\cdot V_{\text{ref}}(s)-\frac{1}{G_{\text{ref}}(s)H_{\text{fb}}(s)+s^2}\cdot F(s) \tag{33}$$

From formula (33), it can be seen that the output signal is only related to the system set value and disturbance term. Therefore, it can be concluded that the transfer function between the output signal of the SC-LADRC system and the interference signal is:

$$\Phi_{\text{SC}}(s)=\frac{Y(s)}{F(s)}=\frac{s^3+C_1s^2+C_2s}{s^5+D_1s^4+D_2s^3+D_3s^2+D_4s+D_5} \tag{34}$$

In equation (34), the coefficients of the numerator and denominator can be specifically expressed as:

$$\begin{cases}C_1=2\omega_{\text{o}}+k_{\text{d}}\\ C_2=\omega_{\text{o}}^2+2\omega_{\text{o}}k_{\text{d}}+k_{\text{p}}\\ D_1=3\omega_{\text{o}}+k_{\text{d}}\end{cases}\qquad\begin{cases}D_2=3\omega_{\text{o}}^2+3\omega_{\text{o}}k_{\text{d}}+k_{\text{p}}\\ D_3=3\omega_{\text{o}}k_{\text{p}}+3\omega_{\text{o}}^2k_{\text{d}}+\omega_{\text{o}}^3\\ D_4=3\omega_{\text{o}}^2k_{\text{p}}+k_{\text{d}}\omega_{\text{o}}^3\\ D_5=k_{\text{p}}\omega_{\text{o}}^3\end{cases}$$

Similarly, the transfer function between the output signal of the TR-LADRC system and the interference signal is:

$$\Phi_{\text{TR}}(s)=\frac{(s+\omega_{\text{o}})^2s+3\omega_{\text{o}}s(s+2\omega_{\text{c}}+\omega_{\text{o}})}{(s+\omega_{\text{o}})^3(s+\omega_{\text{c}})^2} \tag{35}$$

To ensure the fairness of the comparison, the same controller bandwidth parameters and observer bandwidth parameters are selected for the SC-LADRC and TR-LADRC control systems, where the controller bandwidth $\omega_c = 50\text{rad} \cdot \text{s}^{-1}$ is kept unchanged. The observer parameters ω_o of the two systems are simultaneously changed to 250 rad $\cdot$ s^{-1}, 400 rad $\cdot$ s^{-1}, and 550 rad $\cdot$ s^{-1}, and the frequency domain curves of the disturbance rejection performance are plotted as shown in Figure 7.

As can be seen from Fig. 7, in the low-frequency band, there is a large gap in the response of the two system outputs to disturbances. The traditional strategy has a larger response amplitude when ω_o is 250 rad $\cdot$ s^{-1}, 400 rad $\cdot$ s^{-1}, and 550 rad $\cdot$ s^{-1}, which are -103 dB, -108 dB, and -112 dB, respectively, indicating that it is more sensitive to disturbances. In contrast, the response amplitudes of SC-LADRC under three bandwidth values are -146 dB, -155 dB, and -161 dB, respectively, which are smaller than the traditional control strategy, indicating that SC-LADRC has a stronger ability to suppress disturbances. In the mid-frequency band, the response amplitudes of the classic control strategy under three bandwidth values are -76 dB, -80 dB, and -84 dB, respectively, and the response amplitudes of the improved control strategy based on observed state correction are -85 dB, -94 dB, and -100 dB, respectively, indicating that the improved strategy has better anti-disturbance performance In the high-frequency band, the response amplitudes of the two control strategies are close, and the anti-disturbance effect depends more on ω_o. Comprehensive analysis shows that the disturbance suppression performance of SC-LADRC is better than that of TR-LADRC.

D. ROBUST PERFORMANCE ANALYSIS

Considering the perturbation of the internal parameters of the converter and the ADRC, the coefficient matrix of the controlled object becomes $\mathbf{B_1} = [0\ b\ 0]^{\mathrm{T}}$. At this time, by combining equations (13) and (32), we can obtain the frequency domain relationship of y with respect to v_{ref} and f under internal parameter perturbation:

$$Y(s) = \frac{b \cdot k_p G_{\text{ref}}(s)}{b_0 s^2 + bG_{\text{ref}}(s)H_{\text{fb}}(s)} V_{\text{ref}}(s) + \frac{b_0}{b_0 s^2 + bG_{\text{ref}}(s)H_{\text{fb}}(s)} F(s) \tag{36}$$

Define the observer normalized gain parameter $\Delta P_\omega = \omega_o \omega_c^{-1}$ and the converter composite element parameter $\Delta P_b = b_0 b^{-1}$, ΔP_ω represents the relative multiple between the observer and controller bandwidth parameters, and ΔP_b represents the amplitude of the estimated parameter b_0 offset from the actual value b. Substituting parameters ΔP_ω and ΔP_b into $G_{\text{ref}}(s)$ and $H_{\text{fb}}(s)$, and then connecting equation (36) in parallel, we can obtain the transfer function of BDC system output signal with respect to the total disturbance under the perturbation of the internal parameters of the system:

$$\Psi_{b\omega}(s) = \frac{\omega_o^2 (s+\omega_o)^3}{L_1 s^5 + L_2 s^4 + L_3 s^3 + L_4 s^2 + L_5 s + L_6} \tag{37}$$

In equation (37), the coefficients of the numerator and denominator can be specifically expressed as:

$$\begin{cases} L_1 = \Delta P_b \cdot \Delta P_\omega^2; \\ L_2 = \Delta P_b \cdot \omega_o (2\Delta P_\omega^2 + 2\Delta P_\omega) + \omega_o \Delta P_\omega^2 \\ L_3 = \Delta P_b \cdot \omega_o^2 (\Delta P_\omega^2 + 4\Delta P_\omega + 1) + \omega_o^2 (2\Delta P_\omega^2 + 2\Delta P_\omega) \\ L_4 = \omega_o^3 (\Delta P_\omega^2 + 6\Delta P_\omega + 3); \\ L_5 = \omega_o^3 (2\omega_o \Delta P_\omega + 3\omega_o); L_6 = \omega_o^5 \end{cases}$$

For equation (37), the observer gains $\omega_o = 100\text{rad} \cdot \text{s}^{-1}$ and $\Delta P_\omega = 5$ are fixed, ΔP_b is continuously increased, and the Nyquist curve is plotted as shown in Figure 8(a). The observer gains $\omega_o = 100\text{rad} \cdot \text{s}^{-1}$ and $\Delta P_b = 2$ are fixed, ΔP_ω is continuously increased, and the Nyquist curve

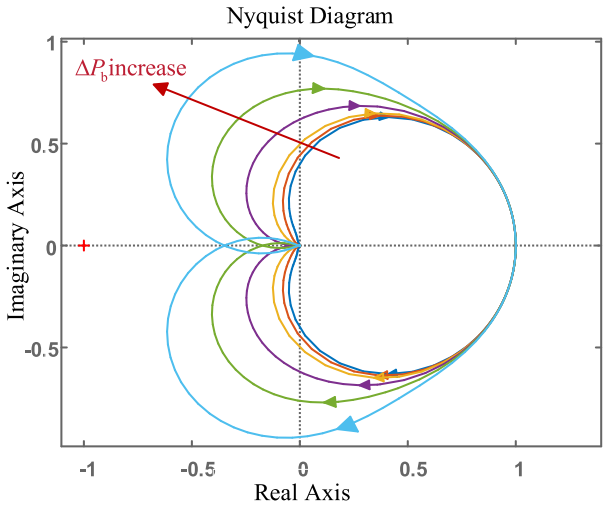

(a) ΔP_b perturbation

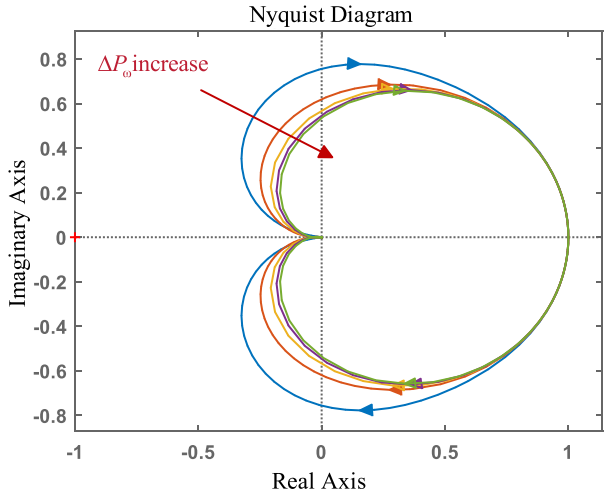

(b) ΔP_ω perturbation

FIGURE 8. The influence of irregular perturbation of internal parameters on system stability.

TABLE 2. System model parameter settings.

Parameters	Value	Parameters	Value
DC bus voltage v_d /V	400	Photovoltaic rated output power/kW	25
Filter inductance L /μH	6800	Supercapacitor rated capacity/Ah	120
HES side capacitor C_1 /μF	6.66	Supercapacitor initial SOC/%	65
Bus side capacitor C_2 /μF	480	Battery rated capacity/Ah	140
Load power/W	2500	Battery initial SOC/%	80

TABLE 3. Detailed values of design parameters in three control systems.

System	LESO Parameters/ rad · s^{-1}	LSEF Parameters/ rad · s^{-1}
TR-LADRC	$\beta_{T1}=7.5\times10^3$ $\beta_{T2}=1.875\times10^7$ $\beta_{T3}=1.5625\times10^{10}$	
CA-LADRC	$\beta_{C11}=\beta_{C21}=7.5\times10^3$ $\beta_{C12}=\beta_{C22}=1.875\times10^7$ $\beta_{C13}=\beta_{C23}=1.5625\times10^{10}$	$k_p=2.5\times10^5$ $k_d=1\times10^3$
SC-LADRC	$\beta_{R1}=5\times10^3$ $\beta_{R2}=6.25\times10^6$ $\beta_{R3}=2.5\times10^3$	

is plotted as shown in Figure 8(b). Then, the influence of the BDC circuit on the stable operation of the system under the irregular perturbations of ΔP_b and ΔP_ω is observed.

As shown in Fig. 8 (a), the increase of ΔP_b is accompanied by a certain degree of deterioration in the stability performance of the system. However, when the value of ΔP_b is in the range of [0.1, 4], the system Nyquist curve does not surround the point (−1, j0), indicating that the system is very tolerant to b, and b is determined by the internal component parameters L, C_1, C_2 of the converter, which also shows that the system has a stronger tolerance to the perturbation of the internal components. As shown in Fig. 8 (b), as the value of ΔP_ω increases, the system Nyquist curve does not surround the point (−1, j0), and is increasingly far away from the point (−1, j0), indicating that the increase of ΔP_ω is accompanied by the enhancement of the stability performance of the system. The system is more tolerant to ΔP_ω, which also shows that the system is more robust to the value of parameter ω_o and ω_c itself. In summary, the SC-LADRC strategy has a strong tolerance to parameter perturbations, that is, the system has strong robustness.

V. SIMULATION AND EXPERIMENTAL VERIFICATIONS

To verify the effectiveness of the SC-LADRC strategy, a DC microgrid system with a photovoltaic storage unit was built on the MATLAB/Simulink platform. Apply TR-LADRC strategy, CA-LADRC strategy, and SC-LADRC strategy to the HES unit interface BDC circuit, while applying five types of interference to the three systems, namely: sudden increase in photovoltaic output, decrease in photovoltaic output, sudden increase in load power demand, sudden decrease in load power demand, and irregular disturbance of internal component parameters in the BDC circuit. Compare and verify the superiority of the SC-LADRC strategy in anti-disturbance and robustness under the above five disturbance conditions. Finally, further convincing verification will be conducted on the experimental platform. The main parameters of the digital simulation platform system model are shown in Table 2. The SC-LADRC strategy is designed using the parameter setting rules in Section III-C. At the same time, to ensure the fairness of the comparison, the three control systems select the same controller parameters and observer parameters, specifically: $\omega_c = 500\text{rad}\cdot\text{s}^{-1}$, $\omega_o = 2500\ \text{rad}\cdot\text{s}^{-1}$.

Furthermore, based on the parameter configuration rules proposed in Sections III-A and III-C for TR-LADRC and SC-LADRC, the detailed values of the design parameters for the two systems can be calculated as shown in Table 3. In addition, the parameter configuration rules for the two observers in the CA-LADRC strategy are the same as those in the TR-LADRC strategy, and the detailed values of the system design parameters are also shown in Table 3, where β_{C11}, β_{C12}, β_{C13} is the front-end parameter of the CA-LADRC system and β_{C21}, β_{C22}, β_{C23} is the back-end parameter of the CA-LADRC system.

A. PHOTOVOLTAIC OUTPUT POWER FLUCTUATION CONDITIONS

In actual operation, photovoltaics fluctuate due to unstable lighting and temperature, and maintaining stable bus voltage under these conditions is a challenge. Therefore, on the basis of stable operation of the DC microgrid, interference conditions of sudden increase and decrease of 20% in photovoltaic power were introduced at 1.5 s and 2.0 s, respectively. The system responses under two operating conditions are shown in Figures 9 and 10, respectively, including the power regulation response of the HES unit and the DC bus voltage response under three energy storage converter control strategies. Select indicators that can visually display the dynamic characteristics of the system to measure its performance, namely DC bus voltage deviation Δv_d and dynamic adjustment time t_s. The corresponding performance index data comparison under this disturbance condition is shown in Figure 13.

As can be seen from Fig. 9 (a), before 1.5 s, P_{Pv} is less than P_{Load}, and the HES unit needs to generate power ($P_{HES} > 0$) to share the power required by the load, and the state of charge (SOC) shows a downward trend, indicating a discharge state; at 1.5 s, P_{Pv} is greater than P_{Load}. At this time, the HES unit quickly absorbs the remaining power

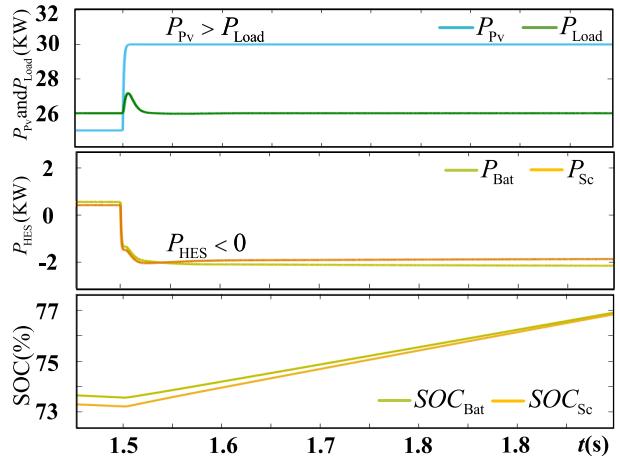

(a) HES output curve

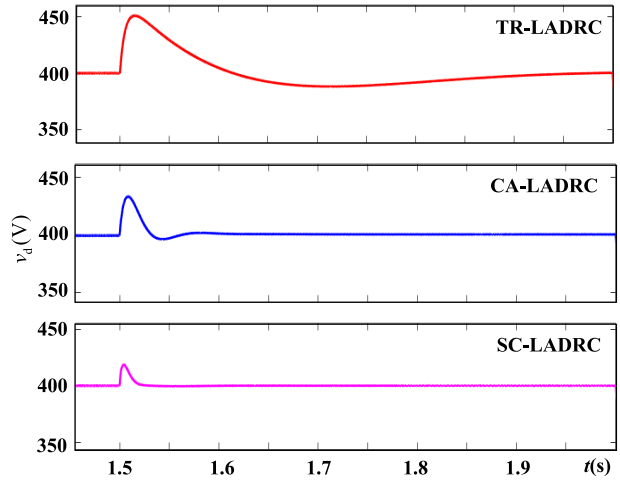

(b) Bus voltage curve

FIGURE 9. Response to sudden increase in photovoltaic output.

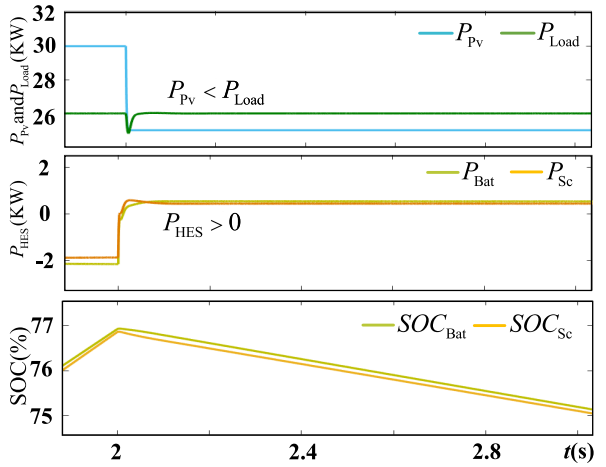

(a) HES output curve

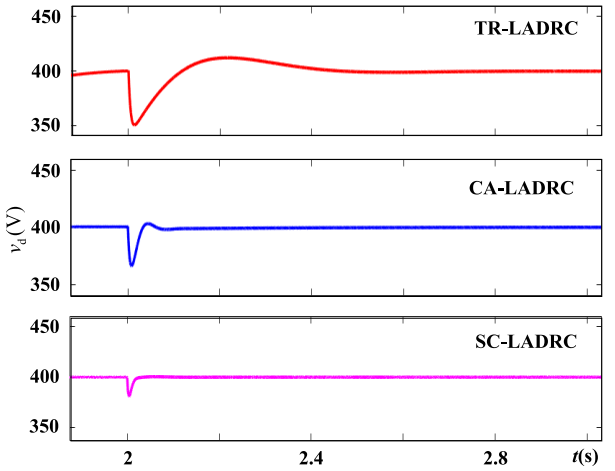

(b) Bus voltage curve

FIGURE 10. Response to sudden drop in photovoltaic output.

of the photovoltaic supported load ($P_{HES} < 0$), and the SOC shows an upward trend, indicating a charging state. It can be seen from Fig. 9 (b) and Fig. 13 that when facing the sudden increase of P_{Pv}, the TR-LADRC system has the longest adjustment time and the largest voltage fluctuation offset, which are 405 ms and 50.8 V respectively. The adjustment time and voltage fluctuation offset of the CA-LADRC system are better than those of traditional control, which are 94 ms and 32.8 V respectively. The SC-LADRC system greatly improves the observation accuracy by compensating for the high-order components in the observer. Compared with the CA-LADRC system, it has more accurate and faster disturbance estimation and compensation performance. The adjustment time and voltage fluctuation offset are 26 ms and 18.8 V respectively. The adjustment time and voltage offset are effectively reduced, achieving deviation and adjustment time better than the TR-LADRC system and CA-LADRC system.

As shown in Fig. 10 (a), before 2 s, the photovoltaic output power is greater than the required power of the load. At this time, the HES unit quickly absorbs the remaining power of the photovoltaic support load ($P_{HES} < 0$), and the SOC shows an upward trend, indicating a charging state. At 2 seconds, the photovoltaic output power drops sharply by 20%, which is not enough to continue to support the load operation. At this time, the HES system can generate power in time ($P_{HES} > 0$) and share the load consumption with the photovoltaic system. The SOC value of the energy storage device decreases, showing a discharged state; combined with Fig. 10 (b) and Fig. 13, it can be seen that among the three control strategies of the HES port converter, the dynamic stability performance of the TR-LADRC system is poor, the voltage offset reaches a high 49.2 V, and the adjustment time is also a long 439 ms; followed by the CA-LADRC system voltage offset and adjustment time are: 33.2 V and 76 ms respectively; whereas the SC-LADRC strategy shows good dynamic stability in both rapidity and deviation, the system voltage offset and adjustment time are: 19.2 V and 26 ms respectively, which is significantly better than the traditional active disturbance rejection control strategy and cascade compensation active disturbance rejection control strategy.

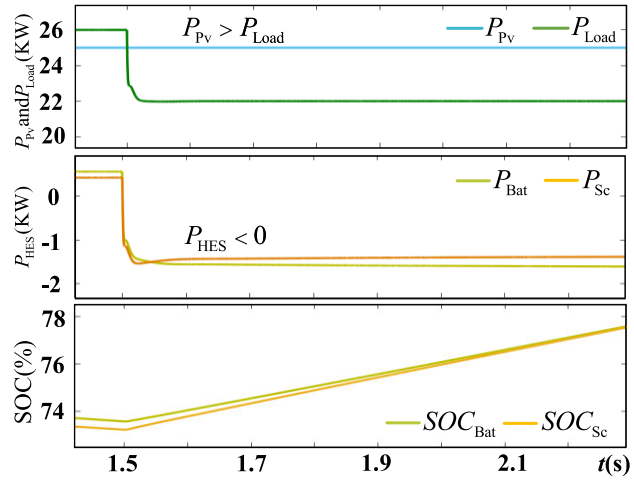

(a) HES output curve

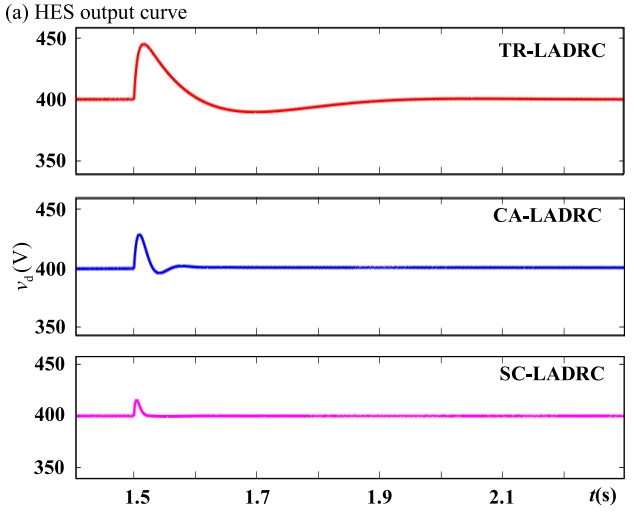

(b) Bus voltage curve

FIGURE 11. Response to sudden drop in load power demand.

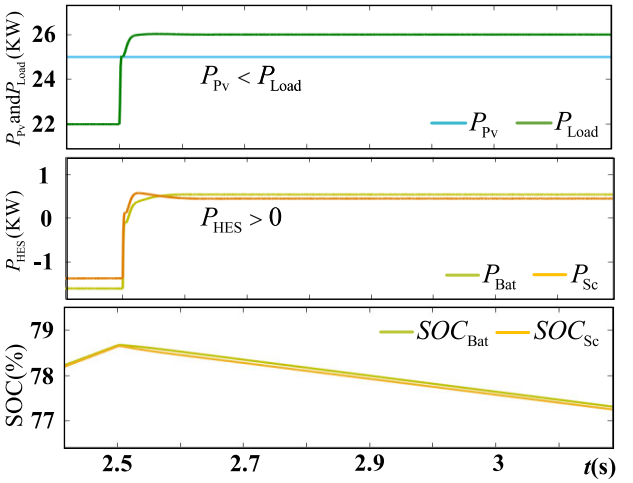

(a) HES output curve

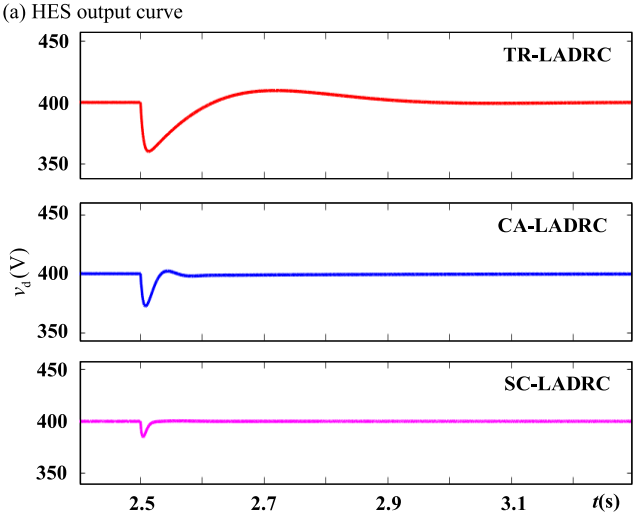

(b) Bus voltage curve

FIGURE 12. Response to sudden increase in load power demand.

B. LOAD POWER CONSUMPTION FLUCTUATION CONDITION

In the actual operation of DC microgrids, the electricity consumption of users on the low or high-voltage load side is uncontrolled, with significant randomness and volatility, causing strong uncertainty in the power demand on the load side. Under this background, controlling the bus voltage to ensure stable operation under these disturbances is of great significance. Therefore, a sudden drop of 15% and a sudden increase of 15% in load power demand are introduced at 1.5 s and 2.5 s of system operation, respectively. The system responses under two operating conditions are shown in Figures 11 and 12, including power regulation of HES and bus voltage response under three energy storage converter strategies. The corresponding indicator data comparison is shown in Figure 13.

As can be seen from Fig. 11 (a), before 1.5 s, the photovoltaic output power is not enough to support the load, so the HES unit sends power ($P_{HES} > 0$) and the photovoltaic power supply together to provide the power required by the load, and the state of charge decreases and is in a discharging state; at 1.5 s, the power required by the load drops below the photovoltaic output, and the photovoltaic power supply itself is sufficient to support the load operation, so the HES unit quickly absorbs the remaining photovoltaic power ($P_{HES} < 0$), and the state of charge increases and is in a charging state. Combined with Fig. 11 (b) and Fig. 13, it can be seen that when facing a significant decrease in load power demand, the voltage offset and regulation time under TR-LADRC are the largest, at 44.8 V and 376 ms, respectively. The CA-LADRC system is second, with voltage offset and regulation time of 28.4 V and 97 ms, respectively. SC-LADRC has the best control effect among the three control strategies because it performs high-precision compensation for the disturbance observation state. The offset and adjustment time are reduced to 15.6 V and 20 ms respectively, which can restore the DC microgrid system to stable operation in the fastest time and with the smallest fluctuation amplitude. The dynamic performance of the energy storage converter has been significantly improved.

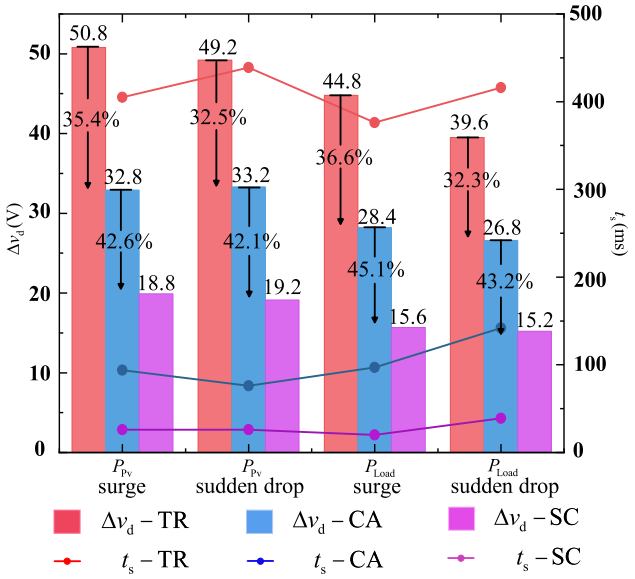

FIGURE 13. Comparison of performance index values under four working conditions.

As can be seen from Fig. 12 (a), at 2.5 s, the load power demand increases, and the photovoltaic output power is insufficient to support the load operation. Therefore, the HES unit quickly outputs power ($P_{HES} > 0$), the state of charge decreases, and it is in a discharging state. Combining Fig. 12 (b) and Fig. 13, it can be seen that when faced with a sudden drop in load demand, the SC-LADRC control strategy can maintain the stable operation of the system at a high speed (39 ms) and a low deviation (15.2 V) due to the high accuracy of the observer.

In summary, when faced with large fluctuations in photovoltaic output and frequent fluctuations in load power demand, the HES unit can quickly supplement the power that photovoltaics cannot provide and absorb the excess power of photovoltaic energy supply, thereby maintaining the power balance of the system; among the three control strategies applied to the HES unit interface converter, the SC-LADRC strategy is significantly better than the TR-LADRC strategy and the CA-LADRC strategy, and can achieve stable control of the bus voltage with smaller overshoot and shorter adjustment time, and has better dynamic performance.

It should be pointed out that when a DC microgrid is disturbed, the bus voltage fluctuation will easily cause system instability when the maximum amplitude exceeds the rated value ±5%, thereby causing the protection device to operate or even load shedding, seriously endangering the normal operation of the large power grid [39]. Observing the bus voltage disturbance waveforms of the DC microgrid in Figures 9 to 12 and the performance index data shown in Fig. 13, it can be seen that when the photovoltaic output fluctuates greatly and a large number of loads are switched, the overshoot of the system under the control of the TR-LADRC strategy and the CA-LADRC strategy is more than ±5%, which is not conducive to maintaining system stability. On the contrary, the SC-LADRC strategy proposed in this paper can effectively reduce the overshoot to below ±5%, which is of great significance for coping with the system stability under complex working conditions of the DC microgrid.

C. IRREGULAR PERTURBATION OF SYSTEM INTERNAL PARAMETERS

In the actual operation of the DC microgrid, the internal components of the converter will cause parameter changes due to the manufacturing process, aging, and other reasons. If the controller has poor robustness, its applicability will be greatly limited. Therefore, two types of disturbances are set to verify the robustness of the improved control strategy: first, keep the internal parameters of BDC unchanged and set the internal bandwidth of LADRC to be irregularly perturbed within ±10% of the optimal value; second, the internal bandwidth of LADRC is kept unchanged, and the internal parameters of BDC(L, C_1,and C_2) are irregularly perturbed within ±20% of the nominal values. The Composite Working Condition Integral of Square Error (CISE) can effectively reflect the comprehensive performance of the system. The numerical mathematical description of the CISE index under α composite working conditions is shown in the formula (38). Draw the CISE index plane images of the system under two operating conditions, as shown in Figure 14. The smaller the plane inclination angle, the stronger the robust performance of the system, and the closer the distance to the horizontal plane, the better the anti-disturbance performance of the system.

$$\mathrm{CISE} = \frac{1}{\alpha} \sum_{0}^{\alpha} \int_{0}^{\infty} e^2(t)\mathrm{d}t \quad (\alpha = 1, 2, 3 \cdots) \tag{38}$$

As can be seen from Fig. 14 (a), when the parameters ω_o and ω_c of the LADRC are irregularly perturbed, the index planes of the three strategies are tilted to a certain extent, but the tilt angle of the SC-LADRC strategy is 2.5°, which is smaller than the tilt angle of 8.5° of the CA-LADRC strategy and much smaller than the 16.6° of the TR-LADRC strategy. At the same time, the distance between the SC-LADRC strategy and the horizontal plane is significantly smaller than that of the TR-LADRC strategy and the CA-LADRC strategy, indicating that the SC-LADRC strategy has significant advantages in robustness and anti-disturbance. As can be seen from Fig. 14 (b) and Fig. 14 (c), when the converter parameters C_1, C_2, and L are irregularly perturbed, the plane tilt angle of the TR-LADRC strategy is the largest and the distance from the horizontal plane is the farthest among the three control strategies. The performance of the CA-LADRC strategy is better than that of the TR-LADRC strategy, and the plane height and tilt angle are much smaller than those of the TR-LADRC strategy. But in comparison, the plane tilt angle is the smallest under the SC-LADRC strategy, which is only 1.04° and 0.015°, and is accompanied by the nearest horizontal plane distance, which represents superior robustness and anti-disturbance performance. This is the optimization

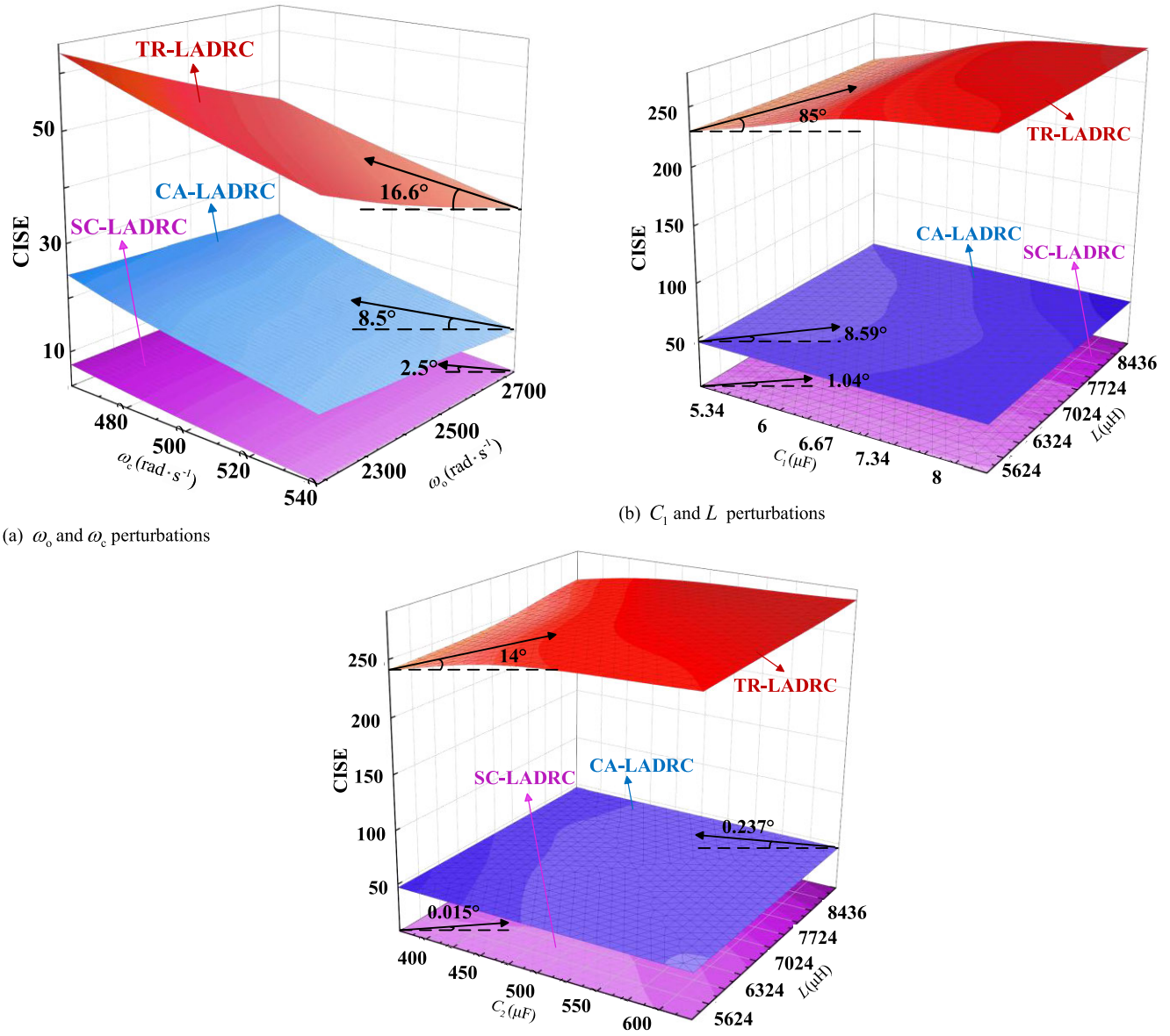

(a) ω_o and ω_c perturbations

(b) C_1 and L perturbations

(c) C_2 and L perturbations

FIGURE 14. Comparison of robustness under irregular perturbations of C_1, C_2 and L.

effect brought about by the introduction of high-order precise compensation terms to improve the accuracy of the observer.

D. EXPERIMENTAL RESULTS

To further validate the effectiveness of the proposed strategy, a small voltage level experimental platform was built for experimental verification. The experimental platform equipment is shown in Figure 15. The platform consists of four core units: BDC and its control circuit, upper computer, programmable power supply, and load module. It also includes three auxiliary units: a digital storage oscilloscope, a load jump switch, and a signal probe. The experimental platform parameters are shown in Table 4.

To verify the improvement effect of the SC-LADRC strategy, TR-LADRC, and SC-LADRC strategies were applied to the BDC control circuit. Due to the sudden change in photovoltaic output causing the energy storage device to operate, resulting in a sudden change in the voltage on the energy storage side, a 20% input voltage mutation is introduced to simplify the simulation of photovoltaic output mutation scenarios. At the same time, a 50% load mutation disturbance condition was introduced, and the system performance was intuitively compared and analyzed through two data indicators: voltage deviation and adjustment time.

In the experiment, a programmable power supply was used to simulate the input voltage jump of the energy storage

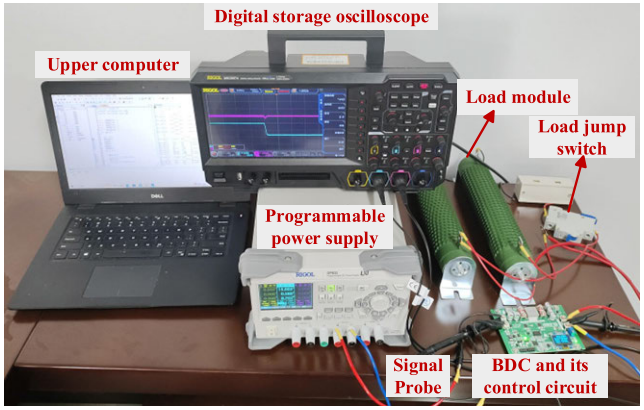

FIGURE 15. Experimental platform for BDC control system of DC microgrid.

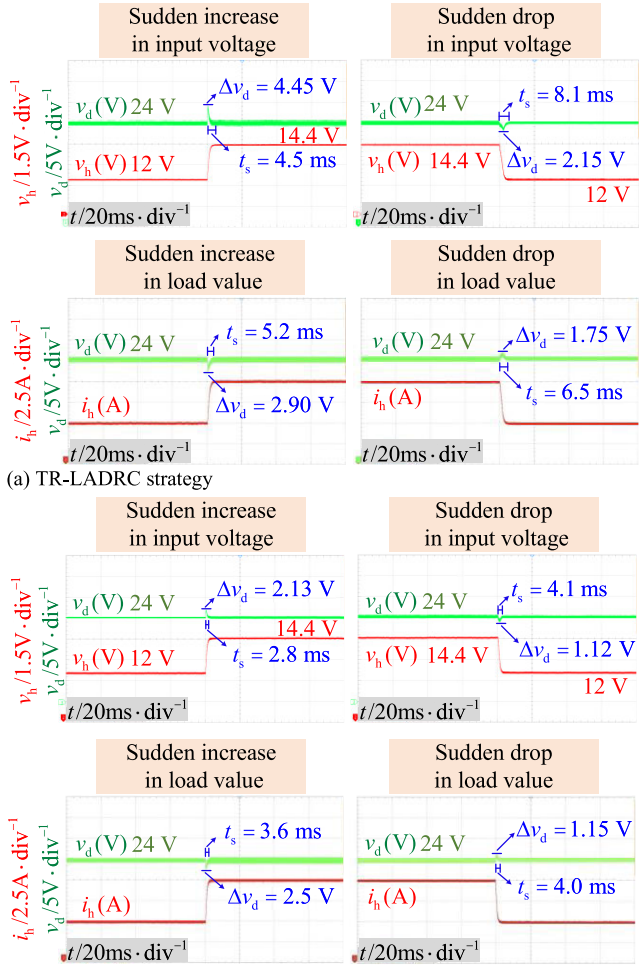

(a) TR-LADRC strategy

(b) SC-LADRC strategy

FIGURE 16. Output waveforms of two control strategies under four different interference conditions.

converter, and a load jump switch was used to simulate the load jump situation. To provide a fair comparison environment, both control strategies were adjusted to the optimal performance. Figure 16 shows the output waveforms of TR-LADRC and SC-LADRC control strategies for the BDC circuit under four different disturbances: sudden increase in input voltage, sudden decrease in input voltage, sudden increase in load value, and sudden change in load value. Two performance indicators, maximum voltage deviation Δv_d and adjustment time t_s, were used to numerically analyze the experimental results.

TABLE 4. Experimental platform parameters.

Parameters	Value	Parameters	Value
Input voltage/V	12	Switching frequency /kHz	200
Output voltage/V	24	Main chip model	STM32F334
Load power /W	115	Switch tube model	BSC070N10NS

From Figure 16, it can be seen that in the face of the same amplitude of input voltage mutation and load mutation disturbance, the voltage deviation and adjustment time under the SC-LADRC strategy are smaller than those under the TR-LADRC strategy. Under four typical disturbance conditions, the absolute value of the voltage deviation can be reduced by an average of 1.0875 V and the adjustment time can be reduced by an average of 2.45 ms compared to the traditional active disturbance rejection strategy. It shows better anti-disturbance performance and dynamic recovery performance in various working conditions. In summary, the SC-LADRC strategy proposed in this article can effectively suppress the adverse effects of external disturbance on the stable operation of DC microgrid systems.

VI. CONCLUSION

In the actual operation of DC microgrids with a high proportion of renewable energy, the voltage and power fluctuations caused by renewable energy are mainly regulated by HES units, and the performance of their interface converters directly affects the voltage stabilization effect of the HES units. To solve this problem, this paper improves the structure based on TR-LADRC and proposes an improved LADRC strategy based on the correction of the total disturbance observation state. Through theoretical, simulation, and experimental analysis and verification, the correctness and effectiveness of the control strategy have been proven, and the following conclusions have been drawn: The SC-LADRC strategy introduces multi-order feedback quantities based on TR-LADRC to reconstruct the disturbance observation state, so that the system has good anti-disturbance and robustness in the face of typical complex working conditions such as large fluctuations in photovoltaic output power, large changes in load-side power demand, irregular perturbations in converter internal parameters, and irregular changes in controller parameters. The performance is significantly better than traditional LADRC and other mainstream improvement strategies, indicating that the SC-LADRC strategy has a more significant voltage stabilization effect on HES port converters and a wider range of applications.

In summary, the SC-LADRC strategy has good engineering application potential in the operation scenarios of DC microgrids with changeable interference and strong

variable coupling. With the continuous expansion of the proportion of new energy, the coupling phenomenon between high-proportion power electronic devices has gradually become an important form of disturbance. Introducing a nonlinear self-disturbance rejection model to suppress the complex physical phenomena caused by strong nonlinear coupling is an important research direction in the field of microgrids. It is hoped that this article can provide more ideas for the stable operation control of various microgrids.

REFERENCES

[1] X. R. Xie, N. J. Ma, W. Liu, W. Zhao, P. Xu, and H. Li, "Functions of energy storage in renewable energy dominated power systems: Review and prospect," *Proc. CSEE*, vol. 43, no. 1, pp. 158–169, Jan. 2023.
[2] X. Zhu, Q. Jiang, and M. Liu, "Two-stage optimal scheduling of integrated energy system considering source-load uncertainty," *Electric Power Autom. Equip.*, vol. 43, no. 8, pp. 9–16, Aug. 2023.
[3] G. F. Hu, Y. Li, Y. J. Cao, and J. J. Zhong, "Multi-time scale optimal scheduling of integrated energy system considering real-time balancing of multi-energy load fluctuation," *Electric Power Autom. Equip.*, vol. 44, no. 5, pp. 120–126, May 2024.
[4] F. F .Chen, L. M. Yang, G. B. Song, Z. Chen, and M. J. Xue, "Overview and prospect of key technologies for active detection protection," *Power Syst. Protection Control*, vol. 51, no. 15, pp. 175–186, Aug. 2023.
[5] Y. W. Zhang, H. T. Hu, A. Q. Geng, J. Y. Chen, Y. B. Ge, and K. Wang, "Capacity optimization configuration of hybrid energy storage system for electrified railway considering peak load shifting," *Electr. Power Automat. Equip.*, vol. 43, no. 2, pp. 44–50, Feb. 2023.
[6] Z. P. Wang and W. Linyf, "Challenges and countermeasures to power system relay protection and safety control," *Power Syst. Protection Control*, vol. 51, no. 6, pp. 10–20, Mar. 2023.
[7] S. Singh, S. Saini, S. K. Gupta, and R. Kumar, "Solar-PV inverter for the overall stability of power systems with intelligent MPPT control of DC-link capacitor voltage," *Protection Control Modern Power Syst.*, vol. 8, no. 1, pp. 245–264, Dec. 2023.
[8] Y. X. Zhong and B. Liu, "Design of micro-grid simulation system based on PID control," *J. New Industrialization*, vol. 9, no. 8, pp. 16–22, Aug. 2019.
[9] W. Haokun, H. Keyuan, L. Wei, M. Xiaoling, and H. Shouduo, "Z-source inverter DC-link voltage control strategy for high speed permanent magnet motor," *Trans. China Electrotechnical Soc.*, vol. 35, no. 16, pp. 3489–3497, Aug. 2020.
[10] C. Ersali, B. Hekimoglu, M. Yilmaz, A. A. Martinez-Morales, and T. C. Akinci, "Disturbance rejecting PID-FF controller design of a non-ideal buck converter using an innovative snake optimizer with pattern search algorithm," *Heliyon*, vol. 10, no. 14, Jul. 2024, Art. no. e34448.
[11] J. Liu, T. Wei, N. Chen, Y. Yin, and W. T. Ng, "A dual-mode digital controller with a high accuracy load current estimator and Gaussian adaptive duty cycle switching for fast transient recovery in DC–DC buck converters," *Comput. Electr. Eng.*, vol. 118, Sep. 2024, Art. no. 109463.
[12] J. Sun, H. He, J. Yi, and Z. Pu, "Finite-time command-filtered composite adaptive neural control of uncertain nonlinear systems," *IEEE Trans. Cybern.*, vol. 52, no. 7, pp. 6809–6821, Jul. 2022.
[13] Z. Yan, S. Deng, Z. Yang, X. Zhao, N. Yang, and Y. Lu, "Improved nonlinear active disturbance rejection control for a continuous-wave pulse generator with cascaded extended state observer," *Control Eng. Pract.*, vol. 146, May 2024, Art. no. 105897.
[14] Y. Wang and H. Liu, "Research on linear/nonlinear active disturbance rejection switching control of PMSM speed servo system," *J. Phys., Conf.*, vol. 2761, no. 1, May 2024, Art. no. 012018.
[15] Z. Hao, Y. Yang, Y. Gong, Z. Hao, C. Zhang, H. Song, and J. Zhang, "Linear/nonlinear active disturbance rejection switching control for permanent magnet synchronous motors," *IEEE Trans. Power Electron.*, vol. 36, no. 8, pp. 9334–9347, Aug. 2021.
[16] Y. Gao, W. Wu, and L. Gao, "Linear active disturbance rejection control for high-order nonlinear systems with uncertainty," *Control Decis.*, vol. 35, no. 2, pp. 483–491, 2020.
[17] Y. Wang, L. Tao, P. Wang, X. Ma, P. Cheng, and D. Zhao, "Improved linear ADRC for hybrid energy storage microgrid output-side converter," *IEEE Trans. Ind. Electron.*, vol. 69, no. 9, pp. 9111–9120, Sep. 2022.
[18] J. Z. Fu, K. L. Guo, and D. Yan, "Research on active disturbance rejection control strategy of bidirectional DC–DC converters in DC microgrid," *Foreign Electron. Meas. Technol.*, vol. 39, no. 3, pp. 47–52, Sep. 2020.
[19] W. Luo and Y. M. Lu, "Compound nonlinear control of multi-level Boost converter with constant power load," *Electric Power Autom. Equip.*, vol. 43, no. 7, pp. 506–512, Jul. 2022.
[20] F. Nejabatkhah and Y. W. Li, "Overview of power management strategies of hybrid AC/DC microgrid," *IEEE Trans. Power Electron.*, vol. 30, no. 12, pp. 7072–7089, Dec. 2015.
[21] C. Ren, Y. Ding, L. Hu, J. Liu, Z. Ju, and S. Ma, "Active disturbance rejection control of Euler–Lagrange systems exploiting internal damping," *IEEE Trans. Cybern.*, vol. 52, no. 6, pp. 4334–4345, Jun. 2022.
[22] J. B. Zhu, F. Li, L. J. Yu, X. L. Li, and C. S. Wang, "Autonomous power mutual support control for AC/DC microgrid interconnected by solid state transformer," *Power Syst. Technol.*, vol. 47, no. 1, pp. 284–295, Jan. 2023.
[23] S. Chen, W. Xue, S. Zhong, and Y. Huang, "On comparison of modified ADRCs for nonlinear uncertain systems with time delay," *Sci. China Inf. Sci.*, vol. 61, no. 7, p. 70223, Jul. 2018.
[24] Y. J. Ma, Y. C. Yuan, X. S. Zhou, X. N. Xu, M. L. Feng, and H. L. Wen, "Model information combined correction active disturbance rejection voltage stabilizing control strategy," *Acta Energi Sin.*, vol. 45, no. 3, pp. 389–398, Mar. 2024.
[25] Q. L. Liu, "Perfotmance analysis and impronement of linear ADRC based on total disturbance," M.S. thesis, School Inf. Control Eng., Qingdao Univ. Technol., Qingdao, China, 2019.
[26] Z. L. Huang, "Control studies of LCL-type grid-connected inverter based on cascade ADRC," M.S. thesis, School Electr. Power Eng., South China Univ. Technol., Guangdong, China, 2021.
[27] L. H. Zhu, G. Q. Zhang, Y. X. Li, G. L. Wang, and D. G. Xu, "Active disturbance rejection control for position sensorless permanent magnet synchronous motor drives based on cascade extended state observer," *Trans. China Electrotechnical Soc.*, vol. 37, no. 18, pp. 4614–4624, Sep. 2022.
[28] C. Wang, K. X. Hou, T. Z. Wu, Q. X. Zhang, and X. X. Zhang, "Dynamic cascade active disturbance rejection-based DC bus stabilizing control for an AC microgrid," *Power Syst. Protection Control*, vol. 52, no. 7, pp. 115–124, Apr. 2024.
[29] Z. J. Liu, X. L. Li, N. Liang, F. Zheng, Y. J. Wu, and T. T. Zhang, "Control strategy of hybrid energy storage for photovolatic microgrid applying feedforward active disturbance rejection," *Electric Power Construct.*, vol. 42, no. 9, pp. 96–104, Sep. 2021.
[30] H. D. Li, S. Q. Xiao, and Y. Jin, "Feedforward active disturbance-ejection control of microgrid bidirectional DC–DC converter based on adaptive PSO," *Electric Mach. Control Application*, vol. 50, no. 2, pp. 73–81, Oct. 2023.
[31] L. Z. Meng, "Research on converters and control strategies of hybrid energy storage system with optical storage and DC microgrid," M.S. thesis, School Elect. Electron. Eng., North China Electric Power Univ., Beijing, China, 2023.
[32] L. Tao, P. Wang, X. Ma, Y. Wang, and X. Zhou, "Variable form LADRC-based robustness improvement for electrical load interface in microgrid: A disturbance response perspective," *IEEE Trans. Ind. Informat.*, vol. 20, no. 1, pp. 432–441, Jan. 2024.
[33] B. B. Li, L. Zeng, P. M. Zhang, and Z. D. Zhu, "Sliding mode active disturbance rejection decoupling control for active magnetic bearings," *Electric Mach. Control*, vol. 25, no. 7, pp. 129–138, Jul. 2021.
[34] Y. L. Zhou, "Improved linear active disturbance rejection control of wind power grid connected inverter under low voltage ride through condition," M.S. thesis, School Elect. Eng. Automat., Tianjin Univ. Technol., Tianjin, China, 2021.
[35] Q. Zheng and Z. Gao, "On practical applications of active disturbance rejection control," in *Proc. 29th Chin. Control Conf.*, Jul. 2010, pp. 6095–6100.
[36] L. Tao, P. Wang, Y. Wang, X. Ma, P. Cheng, and D. Zhao, "Variable structure ADRC-based control for load-side buck interface converter: Formation, analysis, and verification," *IEEE Trans. Ind. Electron.*, vol. 69, no. 6, pp. 6236–6246, Jun. 2022.
[37] Z. Gao, "Scaling and bandwidth-parameterization based controller tuning," in *Proc. Amer. Control Conf.*, 2022, pp. 4989–4996.
[38] Q. Zheng, L. Q. Gaol, and Z. Gao, "On stability analysis of active disturbance rejection control for nonlinear time-varying plants with unknown dynamics," in *Proc. 46th IEEE Conf. Decis. Control*, New Orleans, LA, USA, Dec. 2007, pp. 3501–3506, doi: 10.1109/CDC.2007.4434676.
[39] J. Shi, Z. H. Zheng, and Q. Ai, "Modeling of DC micro-grid and stability analysis," *Electric Power Autom. Equip.*, vol. 30, no. 2, pp. 86–90, Jun. 2010.

XUESONG ZHOU was born in Jiangxi, China. He received the B.S. degree from South China University of Technology, Guangzhou, China, in 1984, and the M.S. and Ph.D. degrees from Tsinghua University, Beijing, China, in 1990 and 1993, respectively. From 1993 to 2002, he worked at Qingdao University, Shandong, China. In 1997, he was promoted as a Professor. Since 2002, he has been a Professor with Tianjin University of Technology, Tianjin, China. His research interests include renewable energy, system control, and smart grids.

YANAN JING was born in Hebei. She received the B.E. degree from the Institute of Disaster Prevention, Langfang, China, in 2017. She is currently pursuing the master's degree in electrical engineering and automation with Tianjin University of Technology. Her current research interest includes complex control technology for new power electronic devices in power systems.

YOUJIE MA was born in Tianjin, China. She received the B.S., M.S., and Ph.D. degrees in electrical engineering from Tsinghua University, Beijing, China, in 1987, 1990, and 1993, respectively. From 1993 to 2002, she worked at the School of Electrical and Automation Engineering, Qingdao University. In 1998, she was promoted as a Full Professor. Since 2002, she has been working as a Distinguished Professor with the School of Electrical and Electronic Engineering, Tianjin University of Technology, Tianjin. Her research interests include power system analysis and automation and smart grids.

XIN WANG was born in Liaoning. He received the B.E. degree from Tianjin University of Technology, Tianjin, China, in 2017, where he is currently pursuing the master's degree in electrical engineering and automation. His current research interest includes intelligent control technology for microgrids.

LONG TAO was born in Hebei, China. He received the B.S. degree in electrical engineering from Tianjin University of Science and Technology, Tianjin, China, in 2017, the M.S. degree in electrical engineering from Tianjin University of Technology, Tianjin, in 2020, and the Ph.D. degree in electrical engineering from Tianjin University, Tianjin, in 2024.

He is currently working as a Lecturer with Tianjin University of Technology. His current research interests include disturbance rejection, multi-energy storage cooperative operation, and application of advanced power electronic technology in microgrids.

HULONG WEN received the M.S. degree from Tianjin University of Technology, Tianjin, China, in 2011. He is currently working as the Research and Development Manager and a Senior Engineer with Tianjin Ruineng Electric. His current research interests include new energy grid connected technology and grid structured wind power converters.